A time-dependent two-dimensional model simulation of lower ionospheric variations under intense SAID

Jun Liang[1], J.P. St-Maurice[2], and E. Donovan[1]

1. Department of Physics & Astronomy, University of Calgary, Canada
2. Institute of Space and Atmospheric Studies, University of Saskatchewan, Canada

Corresponding author: Jun Liang (liangj@ucalgary.ca)

Submitted to Journal of Geophysical Research --- Space Physics

3rd July, 2021

Abstract. The subauroral ion drift (SAID) denotes a latitudinally narrow channel of fast westward ion drift in the subauroral region, often observed during geomagnetically disturbed intervals. The recently recognized subauroral optical phenomena, the Strong Thermal Emission Velocity Enhancement (STEVE) and the Picket Fence, are both related to intense SAIDs. In this study, we present a 2D time-dependent model simulation of the self-consistent variations of the electron/ion temperature, density, and FAC, under strong SAID, with more focus in the lower ionosphere. Our simulation reproduces many key features of SAID, such as the anomalous electron heating in the E-region, the strong electron temperature enhancement in the upper F-region, the intense ion frictional heating, and the plasma density depletion. Most importantly, the ion Pedersen drifts is found to play a crucial role in the density variations and FAC dynamics in the lower ionosphere. The transport effect of ion Pedersen drifts leads to strong density depletion in the lower ionosphere in a large portion of SAID. The FAC inside SAID is mainly downward with magnitude $\leq \sim 1\ \mu A/m^2$. At the poleward edge of SAID, the ion Pedersen drift leads to a pileup of the plasma density and an upward FAC. Our simulation results also corroborate the presence of strong gradients of plasma density, temperature, and flows, at the edge of SAID, which may be conducive to certain plasma instabilities. Our model provides a useful tool for the future exploration of the generation mechanisms of STEVE and Picket Fence.

1. Introduction

During geomagnetically disturbed intervals, a latitudinally narrow yet longitudinally elongated zone of fast westward ion drift (or equivalently strong poleward electric field) often appears in the evening to midnight sector equatorward of the auroral oval. Galperin et al. [1973] first reported such phenomena and called them polarization jets. They were subsequently termed as "subauroral ion drift" (SAID) by Spiro et al. [1979]. References to early observations and to subsequent clarifications of the properties and signatures of SAID can be found in Anderson et al. [1993]. Later, Foster and Burke [2002] suggested an inclusive name, subauroral polarization streams (SAPS), to encompass both the narrow and intense SAIDs and the broader regions of relatively weaker westward subauroral plasma drifts [e.g., Yeh et al., 1991] However, it is now generally recognized that SAID and SAPS (without SAID) differ in a number of fundamental aspects [Mishin et al., 2017; Nishimura et al., 2020]. SAIDs have been studied in both ground and space-based observations, such as in electric field measurements [e.g. Puhl-Quinn, et al., 2007], radar measurements [e.g., Foster et al., 1994], and ion drift measurements [Anderson et al., 1993, 2001; Archer et al., 2018; 2019a; Nishimura et al., 2019; 2020]. Elevated electron/ion temperatures and depleted electron densities are typically observed within SAID [Moffett et al. 1998; Andersen et al., 1993; 2001; Archer et al.,2018; 2019a; Nishimura et al., 2020]. Motivated by the observations, numerous model simulations of the ionosphere have been performed to study the ionospheric processes related to the observed signatures of SAID, for example, the plasma density depletion and electron temperature enhancement in the upper F-region [e.g., Moffett et al., 1992; 1998], and the strong ion upflows in the topside ionosphere [e.g., Heelis et al., 1993].

In recent years, the recognition and observations of the Strong Thermal Emission Velocity Enhancement (STEVE) and the Picket Fence optical phenomena have further lifted the research interest in SAID. The generation mechanisms for the STEVE and Picket Fence remain unclear to date. This stated, it is now well established that STEVE's are collocated with intense SAID channels [Archer et al., 2019a; Nishimura et al., 2019; 2020; Chu et al., 2019], while Picket Fences are situated in close vicinity, likely near the poleward edge, of STEVE [Gillies et al., 2020; Semeter et al., 2020]. The consensus has now emerged that intense SAIDs have to play a pivotal role in the generation of STEVE and Picket Fence optical emissions [Harding et al., 2020; Nishimura et al., 2020; Semeter et al., 2020; Liang et al. 2021]. Important unresolved issues are: (1) a major component of STEVE emissions is not from known atomic or molecular auroral optical emissions but is instead made of a notably very wide broadband emission [e.g., Gillies et al, 2019; Liang et al., 2019]; (2) the green line in the Picket Fence emissions is not accompanied by N_2^+ emissions implying that the emissions may not be generated by an auroral type of electron precipitation [e.g. Mende et al., 2019]. Existing studies on their emission altitudes have unveiled that, the Picket Fence and the lower-altitude part of the STEVE occur in the lower ionosphere (<200 km) [Archer et al., 2019b; Liang et al., 2019; Semeter et al., 2020] and possibly own their production mechanisms to chemical/physical processes in the lower ionosphere [Liang et al., 2019; Hedin et al. 2020; Semeter et al., 2020]. However, despite decades of observations and model simulations of SAID, existing SAID-related studies have been mostly focused on the upper F-region/topside ionosphere, yet the variations/structures in the E-region and lower F-region led by SAID is largely unreported. The lack of definite knowledge about the lower ionospheric variations under intense SAID hampers the exploration of the underlying mechanism of STEVE and Picket Fence.

The present study is motivated by the need to establish the state of the ionosphere in STEVE and Picket Fences situations. A model specially tailored to SAID conditions is built for such a research purpose. We shall investigate the plasma densities, temperatures, conductivities, and electrodynamics in the lower ionosphere under the effect of an intense SAID channel. The plasma densities in the region of interest need to be assessed in the presence of attendant Pedersen currents known to carry plasma across the SAID channels [Banks and Yasuhara, 1978], and in the presence of elevated electron/ion temperatures, including electron temperature enhancements from plasma wave heating in the E region (e.g. St-Maurice and Goodwin [2021], and references therein). The ionospheric variations and structures across the SAID channel achieved from this study would aid in the ongoing exploration of the underlying mechanisms of STEVEs and Picket Fences.

Existing ionospheric models can be broadly categorized into three classes. The first class is a 1D model, e.g., the FLIP model [Richards, 2001], the GLOW model [Solomon et al., 1988], and the now-termed TREx-ATM model [Liang et al., 2016; 2017]. They typically solve the plasma parameters and/or the auroral emission rates along a magnetic field line. The second class is a global 3D model, such as TIEGCM [Richmond et al., 1992], SAMI [Huba et al., 2000], and GITM [Ridley et al., 2002], which typically simulates the evolution and structures of the global or regional ionosphere (and thermosphere) under externally driving forces. However, the time/latitude resolution of those global models is not optimal for our specific research objective, namely the lower ionospheric variations in a narrow SAID channel. The third class of models is often 2D, and typically deals with certain specific small- or meso-scale structures, e.g., a precipitation-enhanced region with sharp boundaries [Noel et al., 2000; 2005; deBoer et al., 2010], the auroral downward current region [Zettergren and Semeter, 2012], and the ionospheric

Alfven resonator [Sydorenko et al., 2013]. A noteworthy effort was done by deBoer et al. [2010], who also incorporated the ion Pedersen drift in their model and highlighted the role of ion Pedersen transport under a tilted field geometry in the lower ionospheric dynamics, though their research interest is focused on the discrete auroral arc with uniform ambient electric field yet sharp precipitation boundary. The model we develop and present in this paper belongs to the third class, and is specifically tailored to intense SAID conditions, with weak precipitation yet strong and narrow electric field structures. Most of the key physical processes that are understood or expected to play a role in SAID, such as the ion Pedersen transport, the anomalous electron heating, the ion upflows, and the enhanced vibrational excitation of N_2, are all incorporated into one synthesized model. The current paper is intended to serve as the first of a series of upcoming studies, based upon the developed model, to investigate more subtleties and anomalies of the ionospheric electrodynamics that could potentially contribute to the STEVE and Picket Fence production under a variety of SAID and ambient ionospheric conditions.

The rest of this paper is organized as follows. In section 2 we describe the basic equations and numerical schemes of our model. In section 3, we depict the ambient ionospheric condition surrounding STEVE that we shall use to set up our model runs. The simulation results are presented in Section 4. We discuss a few important implications of our results in the context of the Picket Fence phenomenon in Section 5 before reaching our conclusions in Section 6.

2. Model description

The model to be described and used in this study inherited from the Transition Region Explorer Auroral Transport Model (TREx-ATM), which we had developed for years [Liang et al., 2016; 2017]. For the specific research purpose of this study, we have made a few key improvements to our previous model: (a) We extend the model to 2D (MLAT/altitude) geometry. (b) We include the electron anomalous heating and the ion Pedersen drift, two pronounced effects of intense SAID in the lower ionosphere, and the FAC is self-consistently computed from the divergence of ion Pedersen currents. (c) In terms of chemical processes, while keeping all ion species and excited neutrals in our previous model, we also consider the change of atomic nitrogen, the nitric oxide, and the vibrational excitation of molecular nitrogen in the model. We emphasize again that the main research interest of this study is in the lower ionosphere (<200 km altitude), which enables us to make a few key assumptions/simplifications of our model. We first introduce the geometry and those key assumptions/simplifications of our model as follows.

1. The SAID plasma convects in the azimuthal (y) direction that is deemed aligned with magnetic L-shell. We assume an azimuthal homogeneity (i.e., $\partial/\partial y = 0$) throughout this study. Anderson et al. [2001] suggested that SAID may exist simultaneously over at least ~3 h MLT. Optical observations of STEVE also indicated that it might span over ~2.5 h MLT sectors [Gallardo-Lacourt et al., 2018b; Nishimura et al., 2020]. Therefore, the timescale of plasma flowing through the SAID is longer than the other timescales of interest, e.g., that of the ion and electron heating, and the density and FAC variation timescale related to the ion Pedersen drift, in the lower ionosphere. That said, the finite azimuthal width of SAID has some effects in the upper ionosphere where the variations tend to be more gradual, and may affect the interpretation of some of our results in the upper F-region, as we shall elucidate later in Section 4.

2. While the electron/ion temperature and density are self-consistently calculated, the major constituents of neutrals (such as $N_2/O_2/O$), as well as the neutral temperature, are kept unchanged in our model. There is little doubt that ionosphere-thermosphere (IT) interaction is operative

under SAID, and there is evidence of such IT interaction based upon neutral observations in conjunction with STEVE [Liang et al., 2021]. However, the coupling to the thermosphere and the resultant change of major neutral constituents would presumably be less important in the lower ionosphere at subauroral latitudes, where the plasma concentration is usually far lower than neutrals. We do include the density variations of some minor neutral species, such as N, NO, and the vibrationally excited N_2 in the model. We assume all neutrals to be stagnant, i.e., we neglect neutral winds.

2.1 Basic equations

In a nutshell, our model consists of the electron and ion energy equations, the continuity equations of ions/electrons as well as some minor and excited neutrals, and the current continuity equation. When the effect of viscous heating is ignored, the electron energy equation is given by [e.g., Rees and Roble, 1975; Schunk and Nagy, 2009],

$$\frac{3}{2}k\frac{D}{Dt}(N_eT_e) = -\frac{5}{2}N_ekT_e\nabla\cdot\mathbf{u}_\mathrm{e} - \nabla\cdot\mathbf{q}_\mathrm{e} + Q_e - L_e \quad , \tag{1}$$

where

$$\frac{D}{Dt} = \frac{\partial}{\partial t} + \mathbf{u}_\mathbf{e}\cdot\nabla \quad ,$$

in which $\mathbf{u}_\mathrm{e}$ is the electron bulk drift velocity, k is the Boltzmann constant, $\mathbf{q}_\mathbf{e}$ is the electron heat flow vector. Q_e is the electron heating rate which, in the context of SAID, consist of three parts: the classical friction heating in both perpendicular directions and parallel directions, the anomalous heating (to be specifically addressed in section 2.2), and the heating due to collisions with secondary electrons produced by the primary auroral precipitation. L_e denotes the electron cooling rate. For detailed breakdown and formulas of all heating/cooling rates and heat flow, see supplementary material. The electron drift $\mathbf{u}_\mathbf{e}$ contains two components: one perpendicular to the ambient magnetic field $\mathbf{u}_{\mathbf{e}\perp}$ and the other parallel to the magnetic field $u_{e//}$. For ionospheric electrons the perpendicular component is essentially E×B convective drift which is virtually incompressible in the ionosphere, so that $\nabla \cdot \mathbf{u}_{e\perp} \approx 0$. The electron Pedersen drift starts to matter at below ~100 km, which is in practice close to the bottom boundary of our model. The explicit expression of $u_{e//}$ is to be given in equation (10) later in this section. Using the continuity equation,

$$\frac{\partial N_e}{\partial t} + \nabla \cdot (N_e \boldsymbol{u}_e) = P_{ne} - L_{ne} \qquad , \tag{2}$$

in which P_{ne} and L_{ne} denote the production and loss of electrons due to precipitations and chemical reactions, equation (1) can be converted to,

$$\frac{3}{2} N_e k \frac{\partial T_e}{\partial t} = -\frac{3}{2} k T_e (P_{ne} - L_{ne}) - \frac{3}{2} N_e k u_{e//} \cdot \nabla_{//} T_e - N_e k T_e \nabla_{//} u_{e//} - \nabla_{//} q_{e//} + Q_e - L_e \ . \tag{3}$$

Note that in our geometry the electron E×B drift is along the y-direction, and $\partial/\partial y = 0$ is assumed in our 2D model, so that the perpendicular advective term vanishes for electrons. Also, we have neglected the perpendicular heat flow component which is usually much smaller than the parallel heat flow for ionospheric electrons [Schunk and Nagy, 2009].

The ion energy equation can be derived similarly,

$$\frac{3}{2} N_i k \frac{\partial T_i}{\partial t} = -\frac{3}{2} k T_i (P_{ni} - L_{ni}) - \frac{3}{2} N_i k \boldsymbol{u}_i \cdot \nabla T_i - N_i k T_i \nabla \cdot \boldsymbol{u}_i + Q_{Ji} - L_{ie} - L_{in} \qquad , \tag{4}$$

in which Q_{Ji} represents the ion heating rate due to the friction Joule heating. L_{ie} and L_{in} represents the cooling rate due to collisions with electrons and neutrals, respectively. Note that in deriving (4) we have also implicitly utilized the ion continuity equation,

$$\frac{\partial N_i}{\partial t} + \nabla \cdot (N_i \boldsymbol{u}_i) = P_{ni} - L_{ni} \ . \tag{5}$$

The ion drift velocity $\mathbf{u_i}$ in equation (4) and (5) is given by

$$\mathbf{u}_i = \frac{\kappa_i^2}{1+\kappa_i^2}\frac{\mathbf{E}\times\mathbf{B}}{B^2} + \frac{\kappa_i}{1+\kappa_i^2}\frac{\mathbf{E}}{B} + \mathbf{u}_{i//} \quad , \tag{6}$$

in which κ_i is the ratio between the ion gyrofrequency and the ion-neutral collision frequency. The ion parallel drift $u_{i_{//}}$ is to be given in equation (9) later. Note that equation (6) represents a stead-state solution of the ion momentum equation. The underlying rationale of such a treatment is that, at the ionospheric altitudes of interest the steady-state ion drift is established at an ion-neutral collisional timescale, much faster than other transport or chemical timescales of interest in our model. Furthermore, the pressure-gradient drifts and diamagnetic drifts are ignored. We infer from our simulation result that, even in the presence of strong heating within SAID, the pressure-gradient associated perpendicular drift is still found to be 3 orders of magnitude smaller than the electric drift, so that the former is ignored. The first two terms on the left-side of equation (6) are conventionally called “Hall drift” and “Pedersen drift”, respectively. As in the case for electrons, the Hall drift does not play a role in the equation under the azimuthally homogeneous geometry. The ion Pedersen drift however, can be very important to the plasma dynamics in the lower ionosphere. As can be inferred from equation (6), the maximum ion Pedersen drift can be up to half the SAID flow velocity. For our research interest of the STEVE-related SAID, whose width is typically no more than a few tens of km, ions traverse the SAID channel in tens of seconds under the enhanced Pedersen drift. This can be faster than the recombination rate of ions in the subauroral ionosphere. Thus, the transport effect led by the SAID-enhanced ion Pedersen drift may act as the principal process controlling the density variations in the lower ionosphere, as first suggested by Banks and Yasuhara [1978]. The

Pedersen drift is dependent upon ion species. In our model, we consider the Pedersen drift of three major ions in the ionosphere, NO^+ , O_2^+, and O^+.

It should be noted that we actually model the so-called "average" ion temperature in equation (4). (a) The temperature is averaged over all ion species. In practical calculation, all heating and cooling sources in equation (5) are summed over ion species, and $\mathbf{u_i}$ in equation (6) represents the density-averaged bulk drift velocity of NO^+ , O_2^+, and O^+. (b) The temperature is averaged over the parallel and perpendicular directions. For more explanations of the implication of such an average ion temperature under frictional heating and its partitioning into parallel and perpendicular directions, see St-Maurice et al. [1999] and Goodwin et al. [2018]. Such an average ion temperature suffices for most of our research purpose (e.g., calculating reaction rates). However, we shall consider the temperature anisotropy and rectify the O^+ $T_{i//}$ when we calculate the ambipolar diffusion velocity (see details later in this section).

We have neglected the ion heat flow conduction in the ion energy equation. The ion heat flow is generally believed to be likely much smaller than the electron heat flow [e.g., Rees and Roble, 1975], though to the authors' knowledge a definite value of the ion heat flux has not yet been reliably evaluated experimentally in the existing literature. It was also ignored in some existing ionospheric models such as TIEGCM [Wang et al., 1999]. As we shall elucidate in the upcoming simulation results, under intense SAID the frictional heating is extremely strong over a broad range of altitudes, and the response time of the ion temperature to the frictional heating is very fast in the lower ionosphere. In fact, T_i is basically determined by a local equilibrium between the frictional heating and the collisional cooling with neutrals over the ionospheric altitudes of interest. We have numerically tested and found that the inclusion of ion heat conduction (as in our previous model Liang et al. [2017]) introduces trivial only changes to the T_i

profile in the lower ionosphere, but incurs heavy computational time costs. Therefore, based upon the above theoretical and practical considerations we ignore the heat conduction in the ion energy equation for the specific purpose of this study.

The parallel electron and ion drifts in equations (3) and (6) are derived from the steady-sate solution (and neglecting advective terms) of the ion and electron momentum equations.

$$-N_i m_i \nu_{in} u_{i//} - N_i m_i \nu_{ie}\left(u_{i//} - u_{e//}\right) - \nabla_{//} p_{i//} - N_i m_i g + N_i e E_{//} = 0 \quad (7)$$

$$-N_e m_e \nu_{en} u_{e//} - N_e m_e \sum \nu_{ei}\left(u_{e//} - u_{i//}\right) - \nabla_{//} p_{e//} - N_e m_e g - N_e e E_{//} = 0 \quad (8)$$

Neglecting terms of the order of m_e/m_i , together with $j_{//} = n_e e\left(\sum u_{i//} - u_{e//}\right)$ these parallel drifts are solved as,

$$u_{i//} = -\frac{g_{//}}{\nu_i} - \frac{\nabla p_{i//}}{N_i m_i \nu_i} - \frac{\nabla p_{e//}}{N_e m_i \nu_i} \quad (9)$$

$$u_{e//} = -\frac{j_{//}}{N_e e} + \frac{\sum N_i u_{i//}}{N_e} \quad (10)$$

in which $g_{//}$ denotes the field-aligned component of the gravitational acceleration. $p_{i//}$ and $p_{e//}$ denote the parallel ion and electron pressure, respectively. The sum in (8) and (10) is over ion species. O^+ is often the dominant ion species in the upper/topside ionosphere where the ambipolar diffusion becomes important, so that in some existing models (such as TIEGCM), only the ambipolar diffusion of O^+ is considered. However, for our specific research interest, NO^+ is found to replace O^+ to become the major constituent in the upper F-region under intense SAID. Therefore, we shall consider two ion species, NO^+ and O^+, for the ambipolar diffusion in our model. For these two ions, their parallel flux $n_i u_{i//}$ is rewritten in the following form,

$$(N_i u_{i//})^{O+} = -g_{i//}\left(\frac{N_i}{\nu_{in}}\right)^{O+} - k \cdot \frac{(\nabla T_{i//})^{O+} + \nabla T_{e//}}{(m_i \nu_{in})^{O+}} (N_i)^{O+} - k \cdot \frac{(T_{i//})^{O+} + T_{e//}}{(m_i \nu_{in})^{O+}} \cdot \nabla (N_i)^{O+} - \frac{k T_{e//}}{N_e (m_i \nu_{in})^{O+}} \cdot \left[(N_i)^{O+} \cdot \nabla (N_i)^{NO+} - (N_i)^{NO+} \cdot \nabla (N_i)^{O+}\right]$$

$$(N_i u_{i//})^{NO+} = -g_{i//}(\frac{N_i}{\nu_{in}})^{NO+} - k \cdot \frac{(\nabla T_{i//})^{NO+} + \nabla T_{e//}}{(m_i \nu_{in})^{NO+}} (N_i)^{NO+} - k \cdot \frac{(T_{i//})^{NO+} + T_{e//}}{(m_i \nu_{in})^{NO+}} \cdot \nabla (N_i)^{NO+} - \frac{kT_{e//}}{N_e (m_i \nu_{in})^{NO+}} \cdot [(N_i)^{NO+} \cdot \nabla (N_i)^{O+} - (N_i)^{O+} \cdot \nabla (N_i)^{NO+}] \quad (11)$$

The superscript in (11) denotes the ion species. We have used the approximation $n_e \approx (n_i)^{NO+} + (n_i)^{O+}$ in the derivation. The calculation of the ambipolar diffusion velocity involves the parallel electron/ion pressure. The electron pressure is assumed to be isotropic in our model. It is however known that ions, especially O^+, can become notably anisotropic in the presence of strong frictional heating [St-Maurice et al., 1999; Goodwin et al., 2018]. More quantitively, Via Monte Carlo simulations Goodwin et al. [2018] showed that, when the ion-ion and ion-electron collisions are considered, the O^+ ion temperature is essentially isotropic for ion drift $u_{i\perp}$< 800 m/s, but the parallel temperature is about half of the average temperature at $u_{i\perp}$~ 4 km/s. In this regard, we use the following empirical formula fitted from the ratio between $T_{i//}$ and the average T_i versus different ion drift velocity for O^+ ions, in the study of Goodwin et al. [2018]:

$$T_{i//}^{O+} = \begin{cases} T_n + (T_i^{ave} - T_n) \cdot [1 - 3.507 \times 10^{-4}(u_{i\perp} - 800) + 6.076 \times 10^{-8}(u_{i\perp} - 800)^2] & u_{i\perp} > 800\, m/s \\ T_i^{ave} & u_{i\perp} < 800\, m/s \end{cases}$$

in which T_i^{ave} represents the average ion temperature solved from equation (4), and T_n is the neutral temperature. For the NO^+ ions, its parallel temperature is much closer to the average temperature. More specifically, even at $u_{i\perp}$ ~4 km/s, contingent on the background neutral concentration the NO^+ parallel temperature is found to be ~80%-86% of the average temperature [Goodwin et al., 2018]. Therefore, NO^+ ion temperature is deemed isotropic in our model.

The FAC is computed according to the current continuity equation,

$$\nabla_{//} \cdot j_{//} + \nabla_{\perp} \cdot (\sum N_i e \mathbf{u}_{\mathbf{i}\perp}) = 0 \quad (12)$$

The existence of FAC and the ambipolar diffusion naturally implies the presence of a parallel electric field $E_{//}$, which can be derived from equation (8). Except for the Alfvenic process which is not considered in our model, the electric field in the ionosphere is essentially electrostatic.

$$\mathbf{E}_{//} = -\nabla_{//}\Phi = \frac{\mathbf{j}_{//}}{\sigma_{//}} - \frac{\nabla_{//}p_e}{N_e e} - \frac{m_e \upsilon_{en}}{N_e e}\sum N_i u_{i//} \quad , \tag{13}$$

$$\mathbf{E}_{\perp} = -\nabla_{\perp}\Phi \tag{14}$$

in which Φ is the electric potential, $\sigma_{//} = N_e e/m_e(\upsilon_{en} + \sum \upsilon_{ei})$ is the parallel conductivity. The electron gravity is ignored here. The last term in (13) is often dismissed in the existing literature [e.g., Schunk and Nagy, 2009] under the assumption that the ion ambipolar drift is much slower than the electron drift as the FAC carrier. This condition may become marginal in intense SAID cases with very strong ion upflows yet moderate FAC intensity [e.g., Heelis et al., 1993; Nishimura et al., 2020]. Such a term is included in our model simulation. The perpendicular electric field would change with the perturbed electric potential. This modifies the ion Pedersen drift and in turn the FAC. Such an interaction/feedback between the electric field and the FAC was found to be capable of generating fine structures of electric fields (including $E_{//}$) under some circumstances [e.g., Noel et al., 2000; deBoer et al., 2010].

Our model also contains 7 excited/minor neutrals (see supplementary material). They all follow the continuity equation in the same format as (2), but without the transport term since no neutral wind is considered in our model. The calculation of the vibrationally excited populations of N_2 will be specifically addressed later in Section 2.3.

Equations (2) through (14) constitute the basic equation set of our model. Except for the anomalous electron heating, which will be specifically discussed in the next subsection, all other heating and cooling rates, as well as all chemical reactions involved in this study, are provided in supplementary material. A special note is given here. Since our research objective features extremely high electron and ion temperatures, and that many reactions are temperature dependent, special care has been taken in checking the validity of empirical formulas of reaction rates at higher electron/ion temperature. In particular, some of the published empirical rates are based upon polynomial fitting of measured data in a certain range of temperature, and may not necessarily guarantee their validity beyond the intended temperature range. Our general scheme is that, if there are several reported empirical formulas with different validity ranges of temperature, we choose to adopt the one that has the highest upper temperature bound and/or is convergent toward high temperature. For example, for the dissociative recombination between O^+ and molecular neutrals, the reaction rates used in this study are from St.-Maurice and Laneville [1998], which remain valid for an effective ion temperature up to ~30000 K. Upon a careful check of all temperature-dependent rates in our model, we notice that many of them are indeed fairly stable toward high temperature, even beyond the labeled upper temperature limit. For a few rate formulas that seem not to be convergent beyond the given upper temperature limit, when the simulated temperature is exceedingly high, we shall use the rate value at the upper temperature limit.

2.2 Anomalous electron heating (AEH)

An accurate calculation of T_e led by AEH is a formidable or even unachievable task at the current stage. First, a rigorous and computationally manageable theory of AEH is still lacking to date. Secondly, existing observations of AEH under very strong convection flows ($V_E > 3$ km/s) are somehow scarce. This is not only because larger V_E is geophysically rare, but also due to that the signal strength may fall below the Incoherent Scatter Radar (ISR) detectability levels due to large electron-ion temperature ratio [Bahcivan, 2007]. Thus, instead of a rigorous theory and solution of AEH, our model goal is to make the best attempts toward a reasonable estimate of T_e in the E-region under intense SAID, based upon available AEH observations.

While it is known that the AEH stems from certain E-region instability/turbulence, the current state of E-region instability theory does not give us accurate spectra of the density and electric field perturbations as a function of the external electric field and ionospheric parameters. Some simplified models of nonlinearly saturated disturbance, albeit all heuristic to a certain degree, were usually applied to evaluate AEH in the E-region ionosphere [e.g., Robinson, 1986; Dimant and Milikh, 2003]. One noteworthy attempt along this route was the Dimant and Mikilh [2003] (hereafter referred to as DM03) model. Though based upon a few heuristic assumptions and simplifications (see Hysell et al. [2013]), the DM03 model has achieved certain success and practical applicability [deBoer et al., 2010; Dimant and Oppenheim 2011a; 2011b; Liu et al., 2016]. For the purpose of this study, we have extensively tested the DM03 model against the realistic AEH events assembled in St-Maurice and Goodwin [2021]. We find that the DM03 results in general show acceptable agreement with realistic observations for convection velocity V_E <2 km/s, but tend to deviate notably from realistic observations for V_E >2 km/s. We footnote that, to the authors' knowledge existing comparisons between AEH theories and observations were usually limited to V_E <2 km/s [Milikh and Dimant 2003; Williams et al., 1992]. St-Maurice and Goodwin [2021] suggested that the anomalous heating rate may be approximated by a 3rd-order polynomial of V_E for V_E <~2 km/s, but is better described by a 4th-order polynomial when V_E is larger. This finding partly explains why the agreement between the simulated T_e and the observations becomes relatively poor at strong V_E (>2 km/s), since the DM03 (and also Robinson [1986]) heating rate basically represents a 3rd-order polynomial of V_E. On the other hand, the DM03 model also incorporates a kinetic modification of the electron cooling rate, which was inferred from a kinetic simulation [Milikh and Dimant 2003] that is not easily replicated in our model.

We elect to resort to the approach of an observation-based empirical model. Recently, the behavior of AEH was revisited by St-Maurice and Goodwin [2021] based upon a rich dataset of realistic observations; a strong tendency of linear dependence of E-region electron temperature versus electric field magnitude is found in their study. A similar conclusion was also reached in Foster and Ericson [2000]. More specifically, St-Maurice and Goodwin [2021] suggest the following empirical formula,

$$T_e = T_{e0} + S \cdot (V_E - 800\mathrm{m/s}) \quad . \tag{15}$$

T_{e0} represents a base level when the AEH is supposed to play little or none effect ----- the instability leading to AEH is supposed to have an E-field threshold, e.g., see equation 14 in DM03). V_E represents that F-region ion flows observed by ISR (evaluated at 300 km altitude). T_{e0} is expected to be event-dependent, contingent upon parameters such as the ambient neutral temperature and other heating/cooling sources at play. In our model, we resolve T_e with all other heating and cooling sources (in the absence of AEH but including the classical frictional heating) for V_E up to 800 m/s, and hereby determine T_{e0}. The slope S used in our model is based upon St-Maurice and Goodwin [2021]; the values in their Table 1 are slightly smoothened and interpolated to our model grids in the 100-120 km altitude range. Figure 1 displays the altitudinal profile of S used in our model. In supplementary material, we provide a simple subroutine that can be used to evaluate the enhancement of T_e under AEH with the convection flow strength V_E, without the necessity of complicated modeling effort. We also point out that, though a complete theory of AEH is unavailable to date, according to existing theories and reasonable theoretical expectations, the AEH heating rate and the dominant cooling terms (elastic and inelastic collisions with neutrals) would presumably all be proportional to the electron density. Therefore, the AEH T_e enhancement is expected to be insensitive to electron density variations [e.g., Liu et al., 2016].

One may question that, since existing AEH observations are generally limited to V_E <3.5 km/s, we may have to assume a linear extrapolation beyond that range. St-Maurice and Goodwin [2021] suggested that the linear trend may sustain to higher V_E, since the aspect angle of the plasma instability structures responsible for the heating is basically proportional to the ambient electric field. Readers are referred to their paper for more theoretical details of their proposal. To partially relieve the uncertainty in extrapolation, in the following run we shall use a peak V_E of ~4 km/s --- this is not up to the extreme SAID events in existing reports, but fairly close to (when mapped to the Swarm altitudes) the median value of Swarm observations of STEVE-related SAID events as reported in Archer et al. [2019a]. Given the current status of AEH theories and observations under intense V_E , it is fair to say that neither a semi-heuristic model approach (such as DM03) nor an empirically data-based approach can be completely free of uncertainty, and it is difficult to assert which approach is inherently better. Anyway, the empirical approach we elect to use is incontrovertibly advantageous in computation efficiency. We have made test runs using DM03 for the AEH module and found that, while the DM03 model may produce somehow different T_e profile in the E-region, the major results of this study, such as the plasma depletion and conductance reduction in the lower ionosphere, are not qualitatively changed.

2.3 Vibrationally excited N_2 distribution

Under SAID, the vibrational excitation of N_2 plays an important role in the electron density depletion in the upper/topside ionospheric altitude where T_e is significantly elevated. In short, N_2^* at higher vibration levels has a much faster reaction rate with O^+ and thus effectively converts O^+ to NO^+. Since NO^+ has a faster recombination rate than O^+, the total plasma density is reduced accordingly. However, as explained in Campbell et al. [2006], a time step simulation is not practical for the calculation of N_2^* populations because the wide range of radiative transition probabilities would require a prohibitively large number of small time intervals. As done in many previous studies [e.g., Cartwright et al., 2000; Campbell et al., 2006], in our model we consider only the steady-state equilibrium distribution of the vibrationally excited N_2 states. The equation for the statistical equilibrium of each vibrational level υ of N_2 is given by,

$$k_{\upsilon 0} n_0 + \sum_K CP_\nu^K + \sum_i A_{i\upsilon} n_i + \sum_i VV_{(\nu\pm1)\nu}^{(i\mp1)i} n_{\nu\pm1} n_{i\mp1} + Q_{\nu+1} n_{\nu+1} = \left(\sum_i A_{\upsilon i} + \sum_K CL_\nu^K + \sum_i VV_{\nu(\nu\pm1)}^{i(i\mp1)} n_i + Q_\nu \right) \cdot n_\nu \quad (16)$$

in which $k_{\upsilon 0}$ denotes the electron impact excitation rate of vibrational level υ (we assume the impact excitation stems from the ground state with density n_0). CP_ν^K and CL_ν^K denote the production and loss rate of vibrational level υ due to chemical reactions. $A_{i\upsilon}$ is the transition probability between the vibrational level υ and i. $VV_{(\nu\pm1)\nu}^{(i\mp1)i}$ is the rate of vibrational exchange where a collision between levels $\nu \pm 1$ and $i \mp 1$ leaves them in level υ and i. Q_ν is the rate of stepwise quenching of level N_2^* by collisions with O atoms. The vibration-translational transition and the molecular diffusion of N_2 are ignored in the model. We consider up to the 10^{th} level of the vibrational N_2 state. For other details of the calculation of N_2^* distribution, see Newton et al. [1974], Cartwright et al. [2000], and Campbell et al. [2006]. The calculation of electron impact excitation, as well as all N_2^*-involved chemical processes and their reaction rates, are identical to those in Campbell et al. [2006]. The vibrational-vibrational exchange rate is from Newton et al. [1974]. The transition probabilities between vibrational levels are from Parlov [1998]. Note that the vibrational excitation of N_2 is also one of the major electron cooling processes, and the cooling rate is self-consistently calculated from the transition probability coefficients in our model.

Once the N_2^* distribution is determined, we use the formula in St.-Maurice and Laneville [1998] for the reaction rate between O+ and ground-state N_2, and use the coefficients in Schmeltekopf et al. [1968] for the relative enhancement of reaction rates at higher vibrational levels of N_2 (see table S3 in supplementary material). An effective reaction rate between O^+ and N_2 is calculated accordingly [e.g., Campbell et al., 2006].

2.4 Numerical Scheme

The energy equations and the continuity equations are solved alternatively using a Strang time-splitting approach. Schematically, T_e and T_i advance at the integer time grid ($t^n \rightarrow t^{n+1}$), while the ion densities of all species and FAC advance at the half-integer time grid ($t^{n-1/2} \rightarrow t^{n+1/2}$). Note that as our convention here the upper script denotes the timestep. A dipole magnetic field configuration is used in the model. The spatial grid is two-dimensional: one along a dipole filed line and equally spaced in the vertical (z) direction, the other horizontally along the magnetic meridian (x-direction, positive northward) and equally spaced in MLAT in the AACGM sense. In all simulation runs presented in this paper, we adopt a time step of 0.1 s. The vertical grid interval is 1 km and the horizontal grid resolution is 0.025^0 MLAT. In such a grid coordinate system, using Jacobi transform we express the parallel and perpendicular gradient operator as $\nabla_{//}= \frac{\partial}{\partial s} = \frac{\partial}{\partial z} sinI$, $\nabla_{\perp}= \frac{\partial}{\partial x} cscI + \frac{\partial}{\partial s} ctgI$, in which I is the magnetic dip angle.

One major challenge in the implementation of our model lies in the dramatic differences among, and the altitudinal variations of, the timescales of the chemical/physical processes involved. To deal with such a difficulty, we use a combination of the steady-state solution, the Runge-Kutta method, and the numerical difference approach, in our numerical scheme. At altitudes below 120 km, the heating rates for both electrons and ions are strong, and the response timescales of T_e and T_i , which are controlled by the electron- and ion-neutral interactions, are very fast (timescale typically on order of ~0.1s or smaller). Therefore, at those altitudes we adopt a steady-state solution for T_e and T_i, For V_E>800 m/s, T_e is obtained from equation (15). For T_e with V_E<800 m/s and T_i, we neglect the time derivative and non-local terms in equations (3) and (4) and jointly solving the two energy equations via Newton's method [Press et al., 2007]. This also sets up the bottom boundary condition for subsequently solving the time-dependent electron/ion energy equations. Note that we still consider the time evolution of the plasma density and FAC at altitudes <120 km, since the chemical reaction timescales and the transport timescale led by the ion Pedersen drift and are typically much longer than 0.1s.

Above 120 km, the time evolutions and non-local transport effect of T_e and T_i are considered. The energy equations are solved using a semi-implicit finite difference method; the involved difference schemes are similar to that in Huba et al. [2000] and Zhu et al. [2016]. Schematically, the model uses the backward difference for the time derivative. Each source term partially containing a linear dependence on the temperature is split into two parts, one with a linear dependence, and the other without the linear dependence. The linear terms are evaluated at the current timestep t^n, while the other terms are evaluated at the previous timestep t^{n-1}. The plasma density involved in the energy equation is taken as the value at the previous half timestep $t^{n-1/2}$. For example, the electron cooling term due to elastic collision with neutrals is expressed as $L_{en} = Q_n\left(N_e^{n-1/2}, T_e^{n-1}\right) \cdot [T_e^n - T_n]$, in which Q_n (N_e, T_e) is a nonlinear function of T_e dependent on neural species [Schunk and Nagy, 2009]. The above semi-implicit method is found to be numerically stable. An upwind difference scheme is used in treating the advective term in the ion/electron energy equation. The electron/ion field-aligned drifts are calculated according to equations (9) and (10). However, the terms involving the temperature gradients in (9) and (10) are dropped in electron/ion energy equations. For the electron energy equation which involves thermal conduction, the upper boundary of our model is set at 800 km altitude, where an external electron heat flow is imposed as the upper boundary condition.

The electron and ion energy equations are weakly coupled via an electron-ion collision term. In the lower ionosphere, the electron-ion collision is fairly minor compared to other heating/cooling terms. In our algorithm, in each time step, T_e and T_i are first solved separately with their own energy equation by using values in the previous time step in the electron-ion collision term. We then adopt an iterative approach to obtain convergent solutions of T_e and T_i , i.e., we replace T_i or T_e in the electron-ion collision term with the last obtained values and iterate. In practice, we find that at most two iterations generally suffice for convergent solutions of T_e and T_i with satisfying precision, namely that the relative difference of T_e and T_i between two successive iterations is smaller than 10^{-5} at all altitudes of interest as our criterion.

The densities of ions and minor neutrals are solved at the half-integer time grid. A similar semi-implicit method is also applied to the continuity equations of ion and neutral species involved (except for the vibrationally excited N_2). We use the backward difference for the time derivative. At each timestep $t^{n+1/2}$, the production rate is evaluated at the previous timestep $t^{n\text{-}1/2}$, while the loss rate is written in the form $L_i = \mathcal{L}N_i = \mathcal{L}(t^{n-1/2}) \cdot N_i^{n+1/2}$. T_e^n and T_e^n obtained at the time step t^n are used in calculating the temperature-dependent reaction coefficients. We take into consideration of the Pedersen drift of NO^+ , O_2^+ , and O^+ in their continuity equations up to 350 km altitudes. We adopt the "donor cell" numerical scheme [Huba et al., 2000] in treating the

Pedersen transport term. For minor ions N^+ and N_2^+ , their chemical loss timescale tends to be shorter than the Pedersen transport, so that we ignore the latter and use the 4th-order Runge-Kutta method to solve their time-evolving continuity equations. While each ion or neutral species is solved separately, we again apply an iterative approach (with similar procedure and criterion to that described for T_e and T_i) to obtain convergent solutions of all densities involved. For the vibrationally excited N_2, we only compute the steady-state solution by solving the equation set (17) via Newton's method. The bottom boundary is set at 90 km. At this altitude, the ionosphere is assumed to be under a steady-state local chemical balance; all transport terms related to the Pederson drift and the ambipolar diffusion are dismissed. The upper boundary condition is to be discussed later in this subsection. As to the boundary conditions in the latitudinal direction, the lower-latitude boundary is set at where V_y is constant zero as per our SAID specification (see equation 19 later), so that the plasma density at this lower boundary is solved in 1D geometry without the Pedersen transport. The unidirectional (always poleward) property of the Pedersen drift and our numerical scheme imply that no poleward boundary condition is required.

The ambipolar diffusion term is discretized using a Keller-box method [Keller, 1970]. The coupling term between the two ion species (the last term in equation 11) is treated via an iterative approach similar to that dealing with the ion-electron coupling in their energy equations. The above numerical scheme is found to be stable, as long as the diffusion coefficient $k(T_{i//} + T_e)/m_i\nu_i$ is not too large. In practice, we limit the upper boundary at 500 km in solving the time-dependent ambipolar diffusion equation of NO^+ and O^+ ions. This is due to both scientific and numerical considerations. We recall that equations (9) and (10) are derived under a steady-sate assumption and with the neglecting of the advective term $(\mathbf{v} \cdot \nabla)\mathbf{v}$ in the momentum equations. At higher altitudes with an increasing magnitude of ambipolar drifts, the above assumptions may become questionable. In SAID/STEVE cases the ion upflows may reach a few km/s [e.g., Nishimura et al., 2020], i.e., be supersonic, in the topside ionosphere, and the ion-ion collision also becomes important at those altitudes. Even if we dismiss the above theoretical complication and adopt equation (9) anyway, the very large diffusion coefficient and ambipolar drift speed at high altitudes impose a serious challenge to the stability of the numeral scheme and considerably increase the computational cost. At last, we emphasize again the main research interest of the current study is in the lower ionosphere (<200 km altitude). A more accurate description of the ionospheric variations and ion upflows in the topside ionosphere under SAID would require a different model, probably involving the full electron/ion momentum equations [e.g., Loranc and St-Maurice, 1994; Sydorenko and Rankin, 2013], which will be left for future studies.

Due to the above considerations, we run the time-dependent continuity equation up to 500 km altitude, with the upper boundary condition specified by $u_{i//}$. The way we specify $u_{i//}$ at the boundary is to be given in section 4.1 when we introduce the model run setup. Beyond 500 km altitude, we continue to calculate the plasma density up to 800 km by assuming a flux conservation $\frac{n_i u_{i//}}{B}$=const, corresponding to a steady-state ionosphere under ambipolar diffusion in the absence of chemical production/loss. With such an assumption, equation (11) consists of coupled first-order ODEs for NO^+ and O^+ densities, which are solved via a Runge-Kutta method starting from 500 km altitude. Extensive numerical tests have been performed and confirmed that, while the uncertainty in the specification of the upper boundary condition for the ion continuity equation would affect the solutions in the upper/topside ionosphere, the main research interest in this study, namely the plasma dynamics in the lower ionosphere and the FAC variations (which is dominantly accumulated in the lower ionosphere), is relatively insensitive to the upper boundary condition.

We solve the FAC via numerical integration,

$$j_{//}(z) = -B \cdot \int_{z_0}^{z} \frac{\nabla_{\perp}\cdot(\sum N_i \mathbf{u}_{\mathbf{i}\perp})}{B sinI} \cdot dz \qquad . \tag{17}$$

The bottom boundary z_0 is set at 90 km. The integral is performed over field-aligned grids, and we adopt the Newton-Cotes formula in the numerical integration [Press et al., 2007]. When $j_{//}$ is evaluated in the topside ionosphere, equation (17) is equivalent to the well-known form of $-\nabla \cdot (\Sigma_p \mathbf{E})$, in which Σ_P is the height-integrated (more precisely field-line-integrated) Pedersen conductance. In this study, both Σ_P and FAC are evaluated up to the altitude of 500 km, i.e., the nominal Swarm satellite altitude, to facilitate comparison with Swarm observations, the main data source of SAID/STEVE to date.

Finally, we shall deal with the perturbation of electric fields due to the rise of the $E_{//}$ (see equation 13). The electric potential perturbation is obtained via a numerical integral along the field line from an upper boundary z_{top} ,

$$\delta\Phi = -\int_{z}^{z_{top}} \left(\frac{\mathbf{j}_{//}}{\sigma_{//}} - \frac{\nabla p_e}{N_e e} - \frac{m_e \nu_{en}}{N_e e} \sum N_i u_{i//} \right) . \frac{dz}{sinI} \qquad . \tag{18}$$

The perturbed perpendicular electric field is then calculated via $\delta\mathbf{E}_{\perp} = -\nabla_{\perp}\delta\Phi$ and applied to adjust the ion Pedersen drift and in turn the FAC. Iteration is made until convergent solutions of $j_{//}$, $E_{//}$ and $\delta\Phi$ are reached at each timestep. z_{top} is set as 500 km altitude in our following run, where the external SAID electric field is imposed. A boundary condition $\delta\Phi$=0 is assumed at 500 km altitude. We have numerically tested with higher upper boundary altitudes of $\delta\Phi$, and find that they produce virtually indiscernible difference to the result. More specifically, changing z_{top} from 500 km to 800 km would result in only ~1% difference to the final FAC outcome.

3. Electron precipitation surrounding SAID/STEVE

To simulate the ionospheric variations under SAID/STEVE, we first need to know the ambient condition of the ionosphere surrounding SAID. SAID/STEVE is located in the nightside subauroral region. However, ionization sources are not entirely absent there. First, even on the nightside the geocorona scattering consistently provides weak ionization sources [Thomas, 1963]. Such nightside ionization sources are considered in our model using the same specification embedded in the TIEGCM and GLOW models [Solomon, 2017]. More importantly, existing observations of STEVE suggested that the electron precipitation is weak but not zero surrounding STEVE. In the following we shall review two such observations in the existing literature, with new datasets and aspects added. The first event was reported by Gallardo-Lacourt et al. [2018a]. Figure 2 shows the POES/NOAA satellite data. The upper panel gives the Total Electron detector (TED) observations of the total electron precipitation fluxes in the whole TED energy range 50 eV-20 keV. It is key to notice that the STEVE arc is located amid a weak (<0.1 erg/cm^2/s) yet non-zero electron precipitation region with increasing fluxes toward higher latitudes. The bottom panel of Figure 2 shows the energy channel of the TED sensors where the differential electron fluxes maximize, which is often used to evaluate the characteristic energy of the electron precipitation. Such max-flux energy bins are found to be relatively stable at ~1-2 keV as the ionospheric footprint of NOAA-17 traverses STEVE.

The other event was reported by Gillies et al. [2019]; their Figure 1 is copied as Figure 2b here. In short, the authors sampled the Transition Region Explorer (TREx) spectrometer measurements on STEVE and its surrounding neighbors. The optical spectrum of STEVE shows a continuous enhancement over its ambient neighbors over a broad range of wavelengths, which constitutes the main source of the STEVE brightness. Our interest here is focused on the small yet distinct peak around 428 nm wavelength that exists in both STEVE and its ambient neighbors. This presumably comes from the 427.8 nm blue-line emission of the N_2^+ 1NG system. Such an emission requires ~19 eV excitation energy, and is thus generally recognized as a sign of auroral electron precipitation. Similar 427.nm emissions are also observed in Liang et al [2019]'s STEVE event. It is important to notice that the STEVE does not show appreciable enhancement over surrounding neighbors in terms of the blue-line intensity, so that the 427.8 nm emissions constitute an ambient background, instead of a characteristic emission line, of STEVE. To view the latitudinal profile of the blue-line emission, we sample the meridional distribution of the 427.8 emission intensity during 0640-0641 UT, when the STEVE was the brightest, from TREx spectrometer data. To calculate the 427.8 nm emission intensity, we subtract the out-of-band spectral intensity, taken as the average in 420-425 nm and 430-435 nm wavelength ranges, from the measured spectra, and then integrate the subtracted spectral intensity in 425-430 nm range. Figure 2c shows the distribution of the obtained 427.8 nm emissions versus MLAT. It is interesting to note that the STEVE arc is located amid an increasing slope (toward north) of the blue-line intensity, which is consistent with the POES/NOAA observation in the previous event.

The above inference that STEVE is located amid a region of weak yet increasing (toward high latitudes) electron precipitation is compatible with some other existing observations. Based on DMSP observations He et al. [2014] and Nishimura et al. [2020] both found that the electron fluxes increase across SAID toward high latitudes. Vis optical data Yadav et al. [2021] found that STEVE is embedded in a region with weak but increasing diffuse emissions toward high latitudes. On the other hand, based on magnetospheric observations Chu et al. [2019] and Nishimura et al. [2019] both noticed that the magnetospheric root of STEVE/SAID is situated in a transition from the plasmapause into the electron plasma sheet, where electron fluxes increase toward tail across the magnetospheric SAID structure. To summarize, existing observations invoke the necessity of the inclusion of electron precipitation into the frame of a SAID model. This is particularly important if one considers the current generator mechanism of SAID, which we shall briefly discuss in Section 5. We emphasize again that the weak electron precipitation surrounding STEVE cannot by itself directly account for the optical brightness of STEVE [Gillies et al., 2019], but whether such weak precipitation may play certain indirect roles [e.g., Chu et al., 2019] in the STEVE mechanism is a pending question to be examined in the future. We also admit that detailed knowledge about the electron precipitation associated with STEVE and Picket Fence is still limited (and to a certain degree controversial) to date, based upon unabundant events, so that our specification of the precipitation profile is not without uncertainty in this study. The ambient electron precipitation is embedded in our model as a necessary yet adjustable component.

4. Model simulation

We now present the model run and the results. We first clarify that, the current paper is mainly intended to introduce our model and demonstrate a few key aspects and results from the new model. We have made many test runs with different specifications and profiles of SAID as well as of the ambient ionosphere, and are convinced that the main results and conclusion of this study are not quantitatively changed. It is however inappropriate to elaborate all those test runs in the current paper. In the interest of brevity we will be content, in this paper, to demonstrate two runs that use typical SAID parameters, leaving for a separate publication a more comprehensive examination of the subtlety of ionospheric dynamics, including certain neutral constituents that may potentially contribute to STEVE, under different SAID and ambient ionospheric/precipitation conditions.

4.1 Model run setup

The ambient and initial conditions of the subauroral ionosphere are set up as follows. We assume a weak yet gradually increasing (from 0.02 to 0.06 erg/cm^2/s across SAID) ambient electron precipitation. The precipitation flux spectrum is assumed to be Maxwellian with characteristic energy of 2 keV. The above specification is partly based upon the realistic observations in Gallardo-Lacourt [2018a]. The Boltzmann transport of precipitating auroral electrons is solved via a two-stream electron transport code [Banks, 1974; Solomon et al., 1988] in our model. The plasma convection is initially set as zero, and the electron heat flow at the upper boundary is initially set as a quiet-time value (2×10^9 eV/cm^2/s, e.g., Fallen and Watkins [2013]). We start from the IRI-2016 model with parameters conformal to the realistic geophysical/geomagnetic conditions in the 10 April, 2018 event [Gillies et al., 2019], and run our model (without flow) to a chemical-diffusion equilibrium, which will be then used as the initial/ambient condition of the subsequent run with SAID.

The latitudinal profile of SAID plasma flows is as follows:

$$V_y = \begin{cases} 0 & x < -d \\ V_{y0}\cos^2\left(\frac{\pi x}{2d}\right) & -d < x < 0 \\ V_{y0}\left[\alpha + (1-\alpha)\cos^2\left(\frac{\pi x}{2d}\right)\right] & d > x > 0 \\ \alpha V_{y0} & x > d \end{cases} \tag{19}$$

in which V_{y0} denotes the peak SAID speed, and d controls the width of the SAID channel. The flow profile is imposed at 500 km altitude and mapped along a dipole field geometry. Note that in our specification there is a constant weaker azimuthal flow, parametrized by a small α, poleward of SAID. This is motivated by the observations that, in many realistic cases, weaker yet nontrivial westward plasma flows were often found to exist immediately poleward of SAID, e.g., Anderson et al. [2001] (see their Figure 1), Archer et al. [2019a] (panel a and b in their Figure 1), Nishimura et al. [2019] (see their Figure 3), and Nishimura et al. [2020] (see their Figure 2). Clues of the existence of such westward flows just poleward of STEVE may also be indirectly hinted from the neutral observations in Liang et al. [2021]. Westward neutral winds were found to be strongly intensified (≥200 m/s) at latitudes higher than STEVE yet remain weak equatorward of STEVE. Upon a reasonable premise that the neutral winds at subauroral latitudes are mainly driven by ion drag, one may infer the existence of nontrivial westward plasma flows of several hundred m/s poleward of STEVE/SAID. The above observations are also consistent with the fact that, during major substorm intervals SAPS-like westward plasma flow enhancements are often found to exist equatorward of auroras and extend to subauroral latitudes [Nishimura et al., 2009; Zou et al., 2012; Lyons et al., 2015]. In the following run we set V_{y0} =4250 m/s, d =0.3^0 MLAT, and α =1/8. The peak SAID velocity is selected here according to the median value of eight Swarm-STEVE conjunctive events in Archer et al. [2019a] (see their Figure 2).

Our model has an electron heat flow as the boundary condition at 800 km altitude. Such a heat flow is set to follow the function form $a + b\cos^2(\pi x/2d)$, with a peak of 2.8×10^{10} eV/cm^2/s at the center (x=0) of SAID and a quiet-time value of 2×10^9 eV/cm^2/s outside SAID ($|x|>d$). The external electron heat flow is so specified that it can reproduce the realistic T_e

observations within intense SAID in the topside ionosphere, as we shall elucidate in the following subsection. The SAID and external heat flow are turned on at *t*=0, and we shall trace the time evolution of the plasma temperature, density, and currents afterward.

The other boundary condition is the ion field-aligned drift at 500 km altitude. We assume $u_{i//}^{500}$ =0 for the ambient ionosphere run. For the SAID run, under the notion that the ion upflows in the upper/topside ionosphere are driven by the frictional heating which, to the first order of approximation, is proportional to V_y^2 [e.g., St-Maurice et al., 1999], we use a heuristic specification for the ion upflows at 500 km altitude. $u_{i//}^{500} = \gamma \cdot V_y^2$. In our following model run the factor γ is set as 3×10^{-5} s/m for O^+ and 2×10^{-5} s/m for NO^+ . Their ratio 1.5 is set according to a rough comparison of their $m_i\nu_{in}$ values in the topside ionosphere. The peak O^+ and NO+ upflow speeds are thus ~540 m/s and ~ 360 m/s in the center SAID at 500 km altitude in our model run.

As afore-mentioned, existing STEVE observations indicate that its azimuthal extension may span over ~2.5h MLT sectors [Gallardo-Lacourt et al., 2018b; Nishimura et al., 2020]. Assuming this represents the azimuthal scale of a SAID segment, a 4250 km/s (at 500 km altitude) SAID flows would have a lifetime of ~9 min in the SAID segment. In other words, any new plasma fed into the SAID channel by the ambient global convection has a duration of no more than ~10 min to undergo SAID-imposed changes, even though the SAID itself may last longer. In practical in-situ observations, contingent upon the relative location of the satellite in the SAID segment, the interaction time between the new plasma's SAID entry and its detection by the satellite is typically limited to several minutes. Certainly, such an interaction time is flow-velocity dependent, and is longer at the edge of the SAID channel. Based on the above considerations, we set the maximum simulation time at latitude x to be 18 min or $L_0/V_y(x)$, whichever is smaller. L_0 is set as 2.5 h MLT, and $V_y(x)$ comes from our SAID profile specification (19). For $t > L_0/V_y(x)$, the ionospheric profiles at the corresponding latitude are deemed to be no longer time-varying.

4.2 Simulation results

Movies showing the full time evolution of T_e, $T_{i,}$, N_e , and **j**, are given in supplementary material. The latitudinal profiles of SAID and the background precipitation are plotted on top for reference. It should be noted that the height profile presented in all movies and subsequent figures actually represents the altitudinal distribution along a magnetic field line. Figures 3 to 5 exemplify the T_e, T_i, and N_e profiles, respectively, at t=0, 30 sec, 2 min, 5 min, 10 min, and 15 min. As one can see from the movie, T_e increases rapidly in the E-region right after the onset of SAID, which indicates the AEH effect. Later on, T_e also increases in the upper F-region, and appears to follow a two-step evolution: first a rapid yet weaker enhancement over a broad range of altitudes, then a stronger yet more gradual enhancement that shows a downward propagation trend from the topside ionosphere. Such a T_e enhancement in the upper F-region is led by heat flux conduction from the topside ionosphere [e.g., Rees and Roble, 1975; Moffett et al. 1998]. As afore-mentioned, when considering the finite azimuthal extension of SAID, contingent upon the azimuthal location of the satellite passage, the plasma captured by the satellite at the peak flow latitude usually undergoes SAID intensification for no more than several minutes. Our simulation indicates that, at t=5 min, the peak T_e at the center latitude of SAID reaches ~7500 K at 500 km altitude, close to the median value of peak T_e enhancements under SAID as reported in Archer et al. [2019a].

As to the ion temperature, T_i dramatically increases due to ion frictional heating. The enhancement first occurs in the lower ionosphere, and quickly expands to higher altitudes. Overall, SAID leads to intense ion frictional heating over a broad range of altitudes. There is a slight decrease of T_i at >300 km altitude after ~2 min, which is due to the adiabatic cooling associated with ion upflows [Wang et al., 2012]. T_i reaches ~16000 K in the lower ionosphere at the center of SAID in our simulation, which is compatible with existing theories and simulations of frictional heating. Assuming a balance between the ion frictional heating and the collisional cooling with neutrals, a simple equation of ion temperature can be written as $T_i = T_n + \frac{\langle m_n \rangle}{3k} V_i^2$ [e.g., St-Maurice et al., 1999], in which $\langle m_n \rangle$ denotes the collision-frequency-weighted averaged neutral mass. In the lower ionosphere where N_2 is the major neutral constituent, V_E ~ 4 km/s would lead to ~18000 K ion temperature according to the above theory. Moffett et al. [1998] also predicted T_i up to ~15000 K in a numerical simulation of SAID with V_E=4 km/s. In an event with T_i measurement onboard DE-2 satellite, Anderson et al. [1991] (see their Figure 1) found that T_i at ~388 km altitude exceeded 10000 K when the SAID V_y reached ~4 km/s. Notwithstanding the uncertainty in T_i measurements by ISR [Akbari et al.; 2017; Goodwin et al., 2018], St-Maurice et al. [1999] reported a case in which T_i obtained from EISCAT observations (though closer to $T_{i//}$ under their radar geometry) exceeded 10000 K in the lower F-region when the convective electric field temporarily reached ~225 mV/m.

We turn next to the plasma density variations under SAID. As one can see from the movie, after the start of SAID, N_e in the E- and lower F-region begins to increase in the poleward portion of the SAID channel and to decrease in the equatorward portion of SAID. As time evolves the equatorward density depletion slowly propagates a bit poleward into the center of SAID, as well as extends upward to higher altitudes. These variations are led by the transport term $\nabla \cdot (N_i \boldsymbol{u}_{pi})$ in the continuity equation. More specifically, $N_i \nabla \cdot \boldsymbol{u}_{pi}$ and $\nabla N_i \cdot \boldsymbol{u}_{pi}$ are both depletion terms in the equatorward side of the SAID channel. With growing density variations the $\nabla N_i \cdot \boldsymbol{u}_{pi}$ term gradually drives the density depletion to the poleward side of SAID (except at the very edge of SAID where the $N_i \nabla \cdot \boldsymbol{u}_{pi}$ term leads to a pileup) as well as upward to higher altitudes, conformal to the $\boldsymbol{u}_{pi}$ direction under a tilted field-line geometry. The role of ion Pedersen drift in depleting the lower ionosphere was initially addressed by Banks and Yasuhara [1978]. The plasma density variation in the lower ionosphere shows the most dynamic change in the first couple of minutes, yet becomes slowly changing and/or relatively stable afterward.

At first sight, the above results appear to be at odds with the simulation results in Noel et al. [2005], Milikh et al. [2006], and Liu et al. [2016], which all predicted an increase of the plasma density in the AEH region due to the decrease of recombination rate of NO^+ with enhanced T_e. However, it is important to note that the effect of ion Pedersen drift and the latitudinal width of the AEH structure were not considered in the above studies. We have made test runs without the ion Pedersen drift, and indeed reproduced that N_e gradually increases in the AEH region. However, when the effects of ion Pedersen drift and narrow width of SAID channel are considered, in the ionosphere E-region where AEH actually operates, the transport effect led by the ion Pedersen drift and its divergence/convergence dominates over the chemical recombination process in terms of their contributions to density variations. As we have mentioned in section 2.1, with their Pedersen drift the E-region ions typically traverse the SAID channel in several tens of seconds, while the recombination timescale of NO^+ is much slower. Using the reaction rate in Parlov [2014], in the AEH region with much elevated T_e (up to ~5000 K) and lowered density, the NO^+ recombination timescale is estimated to be on the order of ~10^3 – 10^4 s. The rapid density depletion in the lower ionosphere is almost purely led by the ion

Pedersen transport effect. We note that density depletion due to a similar process is also reported in Zettergren and Semeter [2012].

The plasma density variations in the upper ionosphere where the ion Pedersen drift vanishes are driven by fundamentally different processes. One well-recognized mechanism of such a plasma depletion in the F-region ionosphere is a conversion from O^+ to NO^+ ions via the reaction,

$$O^+ + N_2 \rightarrow NO^+ + N \quad , \tag{R1}$$

whose reaction rate increases rapidly with enhanced ion temperature and electron temperature [St-Maurice and Laneville; 1998, Moffet et al., 1992b; 1998], causing NO^+ to replace O^+ to become the major ion species in the F-region under strong SAID. Since NO^+ has a faster recombination rate than O^+ --- this is true even under elevated T_e --- the plasma density decreases accordingly. However, it should be noted that such a chemistry-driven density depletion does not work effectively in the lower ionosphere where NO^+ is inherently the dominant ion species. The other important process contributing to the plasma density variations in the upper/topside ionosphere is the ion upflows [Anderson et al., 1991; 1993]. As one can see from the movie and Figure 5, there is a gradual decrease of the F-region peak density at ~300-350 km, which is primarily led by the above-depicted reaction R1. Above 400 km, the density is temporarily enhanced during the first minute, which is driven by the thermal expansion of plasma via upflows under elevated temperature. Later on, as the plasma density continues to drop in the entire F-region, notable density depletion throughout the upper ionosphere becomes evident around the center of SAID after ~2 min, and gradually deepens with time.

Figure 6 demonstrates the altitudinal profile of the densities of N_e, NO^+ , and O^+ at the center (x=0) of SAID at t=0, 1 min, and 5 min, and 10 min. Initially, NO^+ is the dominant ion species in the lower ionosphere, while O^+ is dominant at >250 km height. At t=1 min, NO+ density is enhanced substantially and starts to exceed the O^+ density in the F-region ionosphere due to the reaction R1. The O^+ density continues to drop significantly in the entire upper ionosphere due to a combined effect of the chemical process and the upflow evacuation [Anderson et al., 1991; 1993], and NO^+ becomes the major ion species there, though its density also drops with time in the upper ionosphere due to recombination and upflows. The simulation results predict that N_e in the upper/topside ionosphere would drop to the order of a few 10^3 cm^{-3} at the center of SAID, compatible with existing observations [Archer et al., 2019a; Nishimura et al., 2019; 2020].

Figure 7 shows the altitudinal profile of the Pedersen conductivity at the center of SAID at t=30 sec, 2 min, 5 min, and 10 min. The initial Pedersen conductivity (t=0) is overplotted in a dotted line for reference. Due to the density depletion, the Pedersen conductivity decreases at almost all altitudes of interest, but the conductivity peak is always confined to the lower ionosphere. In terms of the height-integrated Pedersen conductance Σ_P, most of the contributions would come from the lower ionosphere. Movies showing the full time evolution of the MLAT-altitude distribution of the current vectors, as well as of the Σ_P and FAC at 500 km altitude, are given in supplementary material. We demonstrate the latitudinal profiles of Σ_P and FAC at t=0, 30 sec, 2 min, 5 min, and 15 min in Figure 8. Quickly following the start of SAID, Σ_P decreases significantly and drops to very low levels (~0.1 S) in the equatorward and center portion of SAID, yet increases at the poleward edge of SAID. Banks and Yasuhara [1978] reported a similar change of Σ_P in their model. The FAC is initially large upon the incidence of SAID, but quickly decreases in magnitude due to the reduction of Σ_P. We further note that the change of Σ_P and FAC is dynamic in the first 2 minutes elapsed time, but becomes slowly varying after that time and even quasi-stable after ~5 min. This indicates that the conductance drop comes more from the Pedersen-transport-driven density depletion in the lower ionosphere than from the gradual density depletion in the upper ionosphere driven by chemical processes and upflows. When reaching a quasi-steady state, the simulated FAC in a main portion of SAID is downward with magnitude smaller than and/or close to ~1 $\mu A/m^2$ or, compatible with observations [Archer et al., 2019a; Chu et al., 2019; Nishimura et al., 2019; 2020]. We have also made other test runs with stronger SAID V_y magnitude, and noticed that the steady-state downward FAC level is relatively insensitive to the peak flow magnitude. The reason is that, with stronger SAID the ion Pedersen drift is also enhanced, leading to a deeper density depletion in the lower ionosphere and the reduction of Pedersen conductance, so that the FAC level remains more or less the same.

On the other hand, a stronger upward FAC appears at the poleward edge of the SAID channel. We note that many existing proposals of the generation mechanism of SAID postulated the existence of upward FACs at the poleward edge of SAID [e.g., Anderson et al., 1993; 2001; De Keyser et al., 1998]. Such upward FACs were indeed observed near the edge of SAID, and are deemed as related to the Picket Fence phenomenon [Nishimura et al., 2019], though their observed intensity (<1 $\mu A/m^2$) tends to be weaker than that in our simulation (peak at ~2 $\mu A/m^2$). Chu et al. [2019] reported an event (see their Figure 2) that an upward FAC peaked at ~1.2 $\mu A/m^2$ at the poleward edge of SAID. We shall recall that the number of existing events under intense SAID condition and with in-situ FAC measurements remains limited to date, and that the technique to derive FAC density from single-satellite magnetic field measurements relies on a current sheet assumption, whose credibility in the case of small-scale FAC structures is questionable [Forsyth et al., 2017]. The latitudinal scale of the upward FACs in our simulation is <10 km, which is marginal for the single-satellite FAC technique. For reference, existing FAC observations under intense SAID came predominantly from DMSP and Swarm 1 Hz magnetic field data, both of which have a spatial resolution of ~8 km. It is thus not impossible that the existing FAC observations based on single-satellite measurements tend to underestimate the peak upward FAC density. Using high-resolution (50 Hz) Swarm magnetic field data, Nishimura et al. [2019] obtained a much larger FAC density (up to ~10 μA/m^2 spike, see their Figure 2), though the accuracy of the FAC determination at this temporal/spatial scale may be questionable [Forsyth et al., 2017].

The discrepancy between the simulated upward FAC intensity and the realistic observations may also result from uncertainties in our model parameters. Since the upward FAC is contributed by the convergence between the Pedersen current inside the poleward edge of the SAID and that outside the SAID, the overestimation of upward FACs may be relieved in two ways: by adjusting the flow gradient and level surrounding the poleward edge of SAID, and/or by adjusting the ambient Pederson conductance surrounding the poleward edge of SAID. In this paper we only demonstrate the former possibility. In the previous run we assumed a flow of 1/8 the peak SAID speed, or ~530 m/s in practice, poleward of the SAID channel. In the following run, we assume a higher constant flow of 850 m/s (α=1/5 in equation 19) poleward of STEVE. Figure 9 displays the altitude-latitude distribution of N_e and the latitudinal profile of FAC at t=15 min from the new run. The plasma density enhancement and FAC at the poleward edge of SAID become substantially weaker than those in the previous run. The peak upward FAC at the poleward edge of SAID is now limited to <1 μA/m^2. Vice versa, we have also tested the case that the flow magnitude is reduced to zero poleward of STEVE, and found that the resulting upward FAC density rises significantly (peak at ~4.5 μA/m^2, not shown). We thus infer that the upward FAC level is fairly sensitive to the flow condition surrounding the poleward edge of SAID; a moderate relaxing (steepening) of the attenuation edge of SAID would cause a substantial decrease (increase) of upward FAC density there. This shall not be unexpected. A smoother V_y gradient around the edge of SAID imposes double-fold effects on the FAC: in addition to weaker convergence of electric fields, a smoother change of V_y also leads to weaker convergence of ion Pedersen drifts and thus less density buildup, and in turn smaller Σ_P. The FAC is thus expected to vary nonlinearly with the V_y gradient. Some other possible reasons for the discrepancy between our simulated upward FAC intensity and the realistic observations will be discussed in Section 5.

5. Discussion

To date, existing observations and model simulations of SAID-related ionospheric variations have been focused on the upper F-region and topside ionosphere, yet the variations and structures in the E-region and lower F-region ionosphere led by SAID remain largely unexplored. In this study, we present a time-dependent 2D model simulation of self-consistent variations of the electron/ion temperature, density, and FAC, under strong SAID, with main focus in the lower ionosphere. In particular, the ion Pedersen drift and its resultant density and FAC variations are self-consistently incorporated into the model. While some uncertainties admittedly exist due to insufficient observations to date, we have made decent attempts to evaluate the AEH and the ambient precipitation conditions surrounding SAID/STEVE based upon current understanding and available observations. Therefore, we have the ground to believe that our model represents the best effort to date in simulating the dynamic variations and structures in the lower ionosphere under intense SAID. While direct observations of the lower ionospheric variations under SAID are still lacking to date, we expect that some of our model results may be validated by the incoming EISCAT3D observations (to be fully operational in 2022).

Our simulation reproduces many key features of SAID that are consistent with the realistic observations and/or theoretical expectations, such as AEH in the E-region, strong electron temperature enhancement in the upper F-region, intense ion frictional heating, and density depletion in the upper F-region. Most importantly, we highlight the key role of ion Pedersen drifts in the variations of the plasma density, the ionospheric conductance, and the FAC. Existing in-situ FAC observations under intense SAID often allude to much reduced Pedersen conductance within the SAID channel. We confirm in this study that a significant reduction of ionospheric conductance indeed occurs within SAID. Such a reduction of ionospheric conductance is mainly owing to the plasma density depletion in the lower ionosphere led by the transport effect associated with the ion Pedersen drift [Banks and Yasuhara, 1978], rather than driven by chemical processes, as the recombination is slowed down due to the elevated electron temperature. The simulated FAC inside SAID is mainly downward with magnitude $\leq \sim 1\ \mu A/m^2$, compatible with observations, though a stronger upward FAC exists at the poleward edge of SAID.

This study aims to investigate the ionospheric variations under an established SAID, instead of the generation mechanism of SAID. The exact formation mechanism of SAID is not entirely clear to date. The idea of the SAID mechanism being associated with a magnetospheric source acting either as a voltage or as a current generator has been a subject of discussion. Readers are referred to Figueiredo et al. [2004] for a detailed discussion in this regard and arguments for the co-existence of both voltage and current drivers. In our model run, the SAID V_y profile is externally specified, and is thus more aligned with the view of a voltage driver of SAID. Nevertheless, the essence of our study remains valid, namely that the dynamic ionospheric variations and the resulting changes of conductivities under SAID must act in a way to self-consistently adjust the ionospheric current and the E-field, no matter which one is the main driver of the SAID. That said, the potential operation of a current driver may lead to certain possible adjustments to our model. While the downward FAC is carried by proton precipitation and/or outflowing ionospheric electrons, the upward FACs, from a current continuity perspective, should be largely conformal to the suprathermal electron precipitation on top of the ionosphere. As addressed in Section 3, existing observations indicated the presence of electron precipitation surrounding STEVE, particularly in its poleward vicinity (see e.g., Nishimura et al. [2019; 2020]), but the FAC carried by such precipitation is lower than the upward FAC density obtained in our simulation. Via numerical tests, we found that the upward FAC level strongly depends on the V_y gradients at the poleward edge of SAID. To match the observed upward FAC densities, a larger flow magnitude immediately poleward of SAID is needed. This, from a current generator perspective, can be rephrased in a way that the moderate upward FAC modifies the ionospheric convection and result in a smoother flow gradient at the poleward edge of SAID. A refinement of our model to accommodate the possible involvement of a current generator, particularly regarding the upward FAC carried by electron precipitation at the poleward edge of FAC, is currently under way and shall be the content of a separate publication in a near future.

Our simulation results indicate the presence of strong latitudinal gradients of plasma density, temperature, and flows, at the edge of SAID. Figure 10 shows the latitudinal profiles of plasma flows, T_e, T_i, and N_e , averaged over 100-150 km altitudes. As one can see, strong gradients of plasma density, temperature, and flows exist at the edge of SAID. It is interesting to note that the density gradients are stronger at the poleward side of SAID than at the equatorward side. Such density/temperature/flow gradients are hotbeds of a number of plasma instabilities (see Kelley [2009] for a thorough discussion of potential plasma instabilities in the ionosphere). For example, the temperature gradient and density gradient are strong and oppositely directed at ~0.1-0.25^0 poleward of SAID, which is known to be conducive to the temperature gradient drift instability [e.g., Hudson and Kelley, 1976]. Such temperature/density gradients are of course contingent upon the actual SAID profile, and it is not impossible that in some cases the gradients can be even steeper than that presented in our simulation with 0.025^0 MLAT grid resolution. These instabilities may become an intrinsic part of the plasma dynamics at the poleward edge of SAID. We speculate that those instabilities, when well developed, can reach a level that may have macroscopic effects on the plasma distributions and variations. For example, the instabilities at a nonlinear stage may lead to the presence of nonlinear currents ($e\langle\delta N_e \cdot (\delta V_i - \delta V_e)\rangle$), and in turn modify the local FAC configuration [e.g., Dimant and Oppenheim, 2011], which constitute another possible reason for the discrepancy between our modeled and observed FAC intensity at the poleward edge of SAID.

The potential operation of instabilities in the presence of sharp plasma gradients in the lower ionosphere may have particular importance to the Picket Fence phenomenon. Picket Fence occurs at ~100-120 km altitude and is typically found at the poleward edge of STEVE [Semeter et al., 2020; Gillies et al., 2020]. It is dominated by green-line emission (excitation energy 4.19 eV) and also contains some N_2 1PG emissions (7.35 eV), but lacks the blue-line emissions (18.75 eV) [Gillies et al., 2019; Mende et al., 2019]. Clues of electron precipitation were found in association with Picket Fence [Nishimura et al., 2019], but the precipitation fluxes tend to be too weak to directly account for the optical brightness of Picket Fence. A number of researchers suggested the possibility that Picket Fence be generated by suprathermal electrons (≤~10eV) locally accelerated in the lower ionosphere [Mende et al., 2019; Gillies et al., 2020; Semeter et al., 2020]. However, the underlying mechanisms of such local acceleration remain elusive to date. Semeter et al. [2020] suggested that such electron heating mechanisms might be intrinsically related to certain local plasma instabilities at play in the lower ionosphere near the boundary of

SAID, in concert with our above proposal. A dedicated exploration of the possible plasma instabilities is beyond the scope of the current paper and shall be left to future studies. Nevertheless, our results in this study have laid the foundation to, and prepared a quantitative context for, such an exploration in the future.

6. Summary and conclusion

While it is now established that the STEVE and Picket Fence phenomena are inherently related to SAID, existing observations and models related to SAID have been limited to the upper F-region/topside ionosphere. The lack of definite knowledge of the lower ionospheric dynamics under intense SAID hampers the exploration of the underlying mechanism of STEVE and Picket Fence. In this study, we present a 2D time-dependent model simulation of the self-consistent variations of the electron/ion temperature, density, and FAC, under strong SAID, with main focus in the lower ionosphere. We reproduce many known or expected features of SAID, such as AEH in the E-region, strong electron temperature enhancement in the upper F-region, intense ion frictional heating, and plasma density depletion. Most importantly, the inclusion of ion Pedersen drifts is proved to be crucial to the density variations and FAC dynamics in the lower ionosphere. We find that the ionospheric conductance is significantly reduced within SAID, and indicate that the conductance reduction is mainly owing to the plasma density depletion in the lower ionosphere, which is primarily driven by the transport effect of ion Pedersen drifts instead of chemical effects. The simulated FAC inside SAID is mainly downward with magnitude $\leq\sim 1$ $\mu A/m^2$, in line with existing observations. Our simulation also predicts that the plasma density in the lower ionosphere and in turn the Pedersen conductance increase at the poleward edge of the SAID channel, leading to an upward FAC there that is qualitatively consistent with, but tends to be somehow larger than, the realistic observations. Via numerical tests, we note that this upward FAC is sensitive to the flow condition surrounding the poleward edge of SAID. Given the potential limitation (e.g., a current-sheet approximation and latitudinal resolution) of the FAC data drawn from in-situ observations, a moderate discrepancy between the model simulation and the realistic FAC observations should not be deemed unreasonable, though we cannot exclude the possibility that the discrepancy stems from certain limitations of our current model.

One other key aspect of this study is that, our simulation results corroborate the presence of strong gradients of plasma density, temperature, and flows, at the edge of SAID. These gradients are potentially conducive to a number of plasma instabilities. The potential operation of instabilities in the presence of sharp plasma gradients in the lower ionosphere may have particular importance to the Picket Fence phenomena, which are usually found near the poleward edge of STEVE. The simulation results of the plasma dynamics and structures under SAID achieved in this study establish the context of, and pave the road to, a future investigation of the possible plasma instabilities at the edge of a SAID channel, our next-step task to carry on this study.

Acknowledgments. The study is supported by Canadian Space Agency. POES data can be obtained at https://www.ngdc.noaa.gov/stp/satellite/poes/. TREx data in this study can be found at: http://data.phys.ucalgary.ca/sort_by_project/other/publication_datasets/2019GL083272/. We acknowledge useful discussions with Dr. Y. Nishimura, Dr. J. Semeter, Dr. Jing Liu, and Dr. Stan Sazykin (departed).

References.

Akbari, H., Goodwin, L. V., Swoboda, J., St.-Maurice, J.-P., and Semeter, J. L. (2017), Extreme plasma convection and frictional heating of the ionosphere: ISR observations, *J. Geophys. Res. Space Physics*, 122, 7581– 7598, doi:10.1002/2017JA023916.

Anderson, P. C., Heelis, R. A., and Hanson, W. B. (1991), The ionospheric signatures of rapid subauroral ion drifts, *J. Geophys. Res.*, 96(A4), 5785– 5792, doi:10.1029/90JA02651.

Anderson, P. C., D. L. Carpenter, K. Tsuruda, T. Mukai, and F. J. Rich (2001), Multisatellite observations of rapid subauroral ion drifts (SAID), J. Geophys. Res., 106(A12), 29,585–29,599, doi:10.1029/2001JA000128.

Anderson, P. C., W. B. Hanson, R. A. Heelis, J. D. Craven, D. N. Baker, and L. A. Frank (1993), A proposed production model of rapid subauroral ion drifts and their relationship to substorm evolution, J. Geophys. Res., 98(A4), 6069–6078, doi:10.1029/92JA01975.

Archer, W. E., & Knudsen, D. J. (2018). Distinguishing subauroral ion drifts from Birkeland current boundary flows. *Journal of Geophysical Research: Space Physics*, 123, 819– 826.

Archer, W. E., Gallardo-Lacourt, B., Perry, G. W., St.-Maurice, J.-P., Buchert, S. C., & Donovan, E. F. (2019a). Steve: The optical signature of intense subauroral ion drifts. *Geophysical Research Letters*, 46, 6279– 6286. https://doi.org/10.1029/2019GL082687

Archer, W. E., St.- Maurice, J.-P., Gallardo-Lacourt, B. (2019b). The vertical distribution of the optical emissions of a Steve and Picket Fence event. *Geophysical Research Letters*, 46, 10719– 10725, https://doi.org/10.1029 /2019GL084473

Bahcivan, H. (2007), Plasma wave heating during extreme electric fields in the high latitude E region, Geophysical Research Letters, 34 (15). https://doi.org/10.1029/2006GL029236

Banks, P. M., C. R. Chappell, and A. F. Nagy (1974), A new model for the interaction of auroral electrons with the atmosphere: Spectral degradation, backscatter, optical emission, and ionization, J. Geophys. Res.,79(10), 1459–1470, doi:10.1029/JA079i010p01459.

Banks, P.M. and Yasuhara, F. (1978), Electric fields and conductivity in the nighttime E-region: A new magnetosphere-ionosphere-atmosphere coupling effect. Geophys. Res. Lett., 5: 1047-1050. https://doi.org/10.1029/GL005i012p01047

Campbell, L., D. C. Cartwright, M. J. Brunger, and P. J. O. Teubner (2006), Role of electronic excited N_2 in vibrational excitation of the N_2 ground state at high latitudes, *J. Geophys. Res.*, **111**, A09317, doi:10.1029/2005JA011292.

Cartwright, D. C., M. J. Brunger, L. Campbell, B. Mojarrabi, and P. J. O. Teubner (2000), Nitric oxide excited under auroral conditions: Excited state densities and band emissions, J. Geophys. Res., 105, 20,857 –20,867.

Chu, X., Malaspina, D., Gallardo-Lacourt, B., Liang, J., et al (2019). Identifying STEVE's magnetospheric driver using conjugate observations in the magnetosphere and on the ground. *Geophysical Research Letters*, 46.https://doi.org/10.1029/ 2019GL082789.

deBoer, J. D., J.-M. A. Noël, and J.-P. St-Maurice (2010), The effects of mesoscale regions of precipitation on the ionospheric dynamics, electrodynamics and electron density in the presence of strong ambient electric fields, Ann. Geophys., 28, 1345– 1360, doi:10.5194/angeo-28-1345-2010.

Dimant, Y. S., and G. Milikh (2003), Model of anomalous electron heating in the E region: 1. Basic theory, Journal of Geophysical Research: Space Physics, 108 (A9).

Dimant, Y., and M. Oppenheim (2011), Magnetosphere-ionosphere coupling through E region turbulence: 2. Anomalous conductivities and frictional heating, Journal of Geophysical Research: Space Physics, 116 (A09304), doi:10.1029/2011JA016649.

De Keyser, J., M. Roth, and J. Lemaire (1998), The magnetospheric driver of subauroral ion drifts, Geophys. Res. Lett., 25(10), https://doi.org/10.1029/98GL01135.

Fallen, C. T., and B. J. Watkins (2013), Diurnal and seasonal variation of electron heat flux measured with the Poker Flat Incoherent-Scatter Radar, J. Geophys. Res. Space Physics, 118, 5327–5332, doi:10.1002/jgra.50485.

Figueiredo, S., T. Karlsson, and G. T. Marklund (2004), Investigation of subauroral ion drifts and related field-aligned currents and ionospheric Pedersen conductivity distribution, Ann. Geophys., 22, 923–934, doi:10.5194/angeo-22-923-2004.

Forsyth, C., Rae, I. J., Mann, I. R., and Pakhotin, I. P. (2017), Identifying intervals of temporally invariant field-aligned currents from Swarm: Assessing the validity of single-spacecraft methods, J. Geophys. Res. Space Physics, 122, 3411– 3419, doi:10.1002/2016JA023708.

Foster, J. C., and P. J. Erickson (2000), Simultaneous observations of E-region coherent backscatter and electric field amplitude at F-region heights with the Millstone Hill UHF radar, Geophysical Research Letters, 27 (19), 3177-180.

Foster, J. C., and W. J. Burke (2002), SAPS: A new categorization for sub-auroral electric fields, Eos. Trans. AGU, 83(36), 393, doi:10.1029/2002EO000289.

Foster, J. C., M. J. Buonsanto, M. Mendillo, D. Nottingham, F. J. Rich, and W. Denig (1994), Coordinated stable auroral red arc observations: Relationship to plasma convection, J. Geophys. Res., 99(A6), 11,429–11,439, doi:10.1029/93JA03140.

Gallardo-Lacourt, B., Nishimura, Y., Donovan, E., Gillies, D. M., Perry, G. W., Archer, W. E., et al. (2018a). A statistical analysis of STEVE. Journal of Geophysical Research: Space Physics, 123, 9893–9905. https://doi.org/10.1029/2018JA025368

Gallardo-Lacourt, B., Liang, J., Nishimura, Y., and Donovan, E. (2018b). On the origin of STEVE: Particle precipitation or ionospheric skyglow? *Geophys. Res. Lett.*, 45,7968–7973. https://doi.org/10.1029/2018GL078509

Gallardo-Lacourt, B., Nishimura, Y., Lyons, L. R., Mishin, E. V., Ruohoniemi, J. M., Donovan, E. F., Angelopoulos, V., & Nishitani, N. (2017). Influence of auroral streamers on rapid evolution of ionospheric SAPS flows. *Journal of Geophysical Research: Space Physics*, 122, 12,406– 12,420. https://doi.org/10.1002/2017JA024198

Galperin, Y. I., Y. N. Ponomarov, and A. G. Zosinova (1973), Direct measurements of ion drift velocity in the upper atmosphere during a magnetic storm, Kosm. Issled., 11, 273.

Gillies, D. M., E. Donovan, D. Hampton, J. Liang, M. Connors, Y. Nishimura, B. Gallardo-Lacourt, and E. Spanswick, First observations from the TREx Spectrograph: the Optical Spectrum of STEVE and the Picket Fence Phenomena, Geophysical Research Letters, 46. https://doi.org/10.1029/2019GL083272

Gillies, D. M., Liang, J., Donovan, E., & Spanswick, E. (2020). The apparent motion of STEVE and the Picket Fence phenomena. *Geophysical Research Letters*, 47, e2020GL088980. https://doi.org/10.1029/2020GL088980

Goodwin, L. V., J.-P. St.-Maurice, H. Akbari, R. J. Spiteri (2008), Incoherent Scatter Spectra Based On Monte Carlo Simulations of Ion Velocity Distributions Under Strong Ion Frictional Heating, Radio Science, 10.1002/2017RS006468, 53, 3, 269-287.

Harding, B. J., Mende, S. B., Triplett, C. C., & Wu, Y.-J. J. (2020). A mechanism for the STEVE continuum emission. *Geophysical Research Letters*, 47, 2020GL087102. https://doi.org/10.1029/2020GL087102

He, F., X.-X. Zhang, and B. Chen (2014), Solar cycle, seasonal, and diurnal variations of subauroral ion drifts: Statistical results, J. Geophys. Res. Space Physics, 119, 5076–5086, doi:10.1002/2014JA019807.

Heelis, R. A., Bailey, G. J., Sellek, R., Moffett, R. J., and Jenkins, B. (1993), Field-aligned drifts in subauroral ion drift events, J. Geophys. Res., 98(A12), 21493-21499, doi:10.1029/93JA02209.

Huba, J. D., Joyce, G., & Fedder, J. A. (2000). SAMI2 (Sami2 is another model of the ionosphere): A new low - latitude ionosphere model. Journal of Geophysical Research, 105, 23,035‐ 23,054.

Hudson, M. K., and M. C. Kelley (1976), The temperature gradient instability at the equatorward edge of the ionospheric plasma trough, J. Geophys. Res., 81, 3913– 3918.

Hysell, D., R. Miceli, and J. Huba (2013), Implications of a heuristic model of auroral Farley Buneman waves and heating, Radio Science, 48 (5), 527-534.

Kelley, M. C. (2009), The Earth's Ionosphere, Plasma Physics and Electrodynamics, Int. Geophys. Ser., 2nd ed., Elsevier, New York.

Liang J., B. Yang, E. Donovan, J. Burchill, and D. Knudsen (2017), Ionospheric electron heating associated with pulsating auroras: A Swarm survey and model simulation, J. Geophys. Res. Space Physics, 122, 8781–8807, doi:10.1002/2017JA024127.

Liang, J., E. Donovan, B. Jackel, E. Spanswick, *and* M. Gillies (2016), On the 630 nm red-line pulsating aurora: Red-line Emission Geospace Observatory observations and model simulations, J. Geophys. Res. Space Physics, 121, 7988–8012, *doi:*10.1002/2016JA022901.

Liang, J., Donovan, E., Connors, M., Gillies, D., St-Maurice, J. P., Jackel, B., et al. (2019). Optical spectra and emission altitudes of double-layer STEVE: A case study. *Geophysical Research Letters*, 46, 13630– 13639. https://doi.org/10.1029/2019GL085639

Liang, J., Zou, Y., Nishimura, Y., Donovan, E., Spanswick, E., & Conde, M. (2021). Neutral wind dynamics preceding the STEVE occurrence and their possible preconditioning role in STEVE formation. *Journal of Geophysical Research: Space Physics*, 126, e2020JA028505 https://doi.org/10.1029/2020JA028505

Liu, J., W. Wang, M. Oppenheim, Y. Dimant, M. Wiltberger, and S. Merkin (2016), Anomalous electron heating effects on the E region ionosphere in TIEGCM, Geophys. Res. Lett., 43, 2351–2358, doi:10.1002/2016GL068010.

Loranc, M., and St-Maurice, J.-P. (1994), A time-dependent gyro-kinetic model of thermal ion upflows in the high-latitude *F* region, *J. Geophys. Res.*, 99(A9), 17429– 17451, doi:10.1029/93JA01852.

Lyons, L. R., Nishimura, Y., Gallardo-Lacourt, B., Nicolls, M. J., Chen, S., Hampton, D. L., … Angelopoulos, V. (2015). Azimuthal flow bursts in the inner plasma sheet and possible connection with SAPS and plasma sheet earthward flow bursts. *Journal of Geophysical Research: Space Physics*, **120**, 5009– 5021. https://doi.org/10.1002/2015JA021023

MacDonald, E. A., Donovan, E., Nishimura, Y., Case, N., Gillies, D. M., Gallardo-Lacourt, B., et al. (2018). New science in plain sight: Citizen Scientists lead to the discovery of optical structure in the upper atmosphere. Science Advances, 4(3), eaaq0030. https://doi.org/10.1126/sciadv.aaq0030

Mende, S. B., Harding, B. J., & Turner, C. (2019). Subauroral green STEVE arcs: Evidence for low-energy excitation. *Geophysical Research Letters*, 46, 14256–14262. https://doi.org/10.1029/2019GL086145

Milikh, G., and Y. S. Dimant (2003), Model of anomalous electron heating in the E region: 2. Detailed numerical modeling, Journal of Geophysical Research: Space Physics, 108 (A9).

Milikh, G. M., L. P. Goncharenko, Y. S. Dimant, J. P. Thayer, and M. A. McCready (2006), Anomalous electron heating and its effect on the electron density in the auroral electrojet, Geophys. Res. Lett., 33, L13809, doi:10.1029/2006GL026530.

Mishin, E., Nishimura, Y., and Foster, J. (2017), SAPS/SAID revisited: A causal relation to the substorm current wedge, *J. Geophys. Res. Space Physics*, 122, 8516– 8535, doi:10.1002/2017JA024263.

Moffett, R. J., A. E. Ennis, G. J. Bailey, R. A. Heelis, and L. H. Brace (1998), Electron temperatures during rapid subauroral ion drift events, Ann. Geophys., 16, 450 – 459

Moffett, R. J., G. J. Bailey, and B. Jenkins (1992b), Effects of greatly increased O+ loss in the ionospheric F-region, Planet. Space Sci., 40, 1631

Moffett, R. J., R. A. Heelis, R. Sellek, and G. J. Bailey (1992a), The temporal evolution of the ionospheric signatures of subauroral ion drifts. Planet. Space Sci., 40, 663.

Newton, G. P., J. C. G. Walker, and P. H. E. Meijer (1974), Vibrationally excited nitrogen in stable auroral red arcs and its effect on ionospheric recombination, J. Geophys. Res., 79, 3807 – 3818.

Nishimura, Y., Gallardo-Lacourt, B., Zou, Y., Mishin, E., Knudsen, D. J., Donovan, E. F., et al (2019). Magnetospheric signatures of STEVE: Implication for the magnetospheric energy source and inter-hemispheric conjugacy. Geophysical Research Letters, 46. https://doi.org/10.1029/2019GL082460.

Nishimura, Y., Donovan, E. F., Angelopoulos, V., & Nishitani, N. (2020). Dynamics of auroral precipitation boundaries associated with STEVE and SAID. *Journal of Geophysical Research: Space Physics*, 125, e2020JA028067. https://doi.org/10.1029/2020JA028067.

Noël, J., St.-Maurice, J., and Blelly, P. (2000), Nonlinear model of short-scale electrodynamics in the auroral ionosphere. *Annales Geophysicae* **18,** 1128–1144. https://doi.org/10.1007/s00585-000-1128-1.

Noël, J.-M. A., J.-P. S.-Maurice, and P.-L. Blelly (2005), The effect of E-region wave heating on electrodynamical structures, Ann. Geophys., 23, 2081– 2094, doi:10.5194/angeo-23-2081-2005.

Pavlov, A. (2014). Photochemistry of ions at D-region altitudes of the ionosphere: A review. Surveys in Geophysics, 35(2), 259–334.

Pavlov A. V. (1998), New electron energy transfer rates for vibrational excitations of N2 , Ann. Geophys., 16, 176–182.

Press, W. H., S. A. Teukolsky, W. T. Vetterling, and B. P. Flannery (2007), Numerical Recipes 3rd Edition: The Art of Scientific Computing (3rd. ed.). Cambridge University Press, USA.

Puhl-Quinn, P. A., H. Matsui, E. Mishin, C. Mouikis, L. Kistler, Y. Khotyaintsev, P. M. E. Décréau, and E. Lucek (2007), Cluster and DMSP observations of SAID electric fields, J. Geophys. Res., 112, A05219, doi:10.1029/2006JA012065.

Rees, M. H., and R. G. Roble (1975), Observations and theory of the formation of stable auroral red arcs, Rev. Geophys., 13(1), 201–242, doi:10.1029/RG013i001p00201.

Richards, P. G. (2001), Seasonal and solar cycle variations of the ionospheric peak electron density: Comparison of measurement and models, J. Geophys. Res., 106(A7), 12803– 12819, doi:10.1029/2000JA000365.

Richmond, A. D., E. C. Ridley, and R. G. Roble (1992), A thermosphere/ionosphere general circulation model with coupled electrodynamics, *Geophys. Res. Lett.*, **19**, 601–604, doi:10.1029/92GL00401

Ridley,A. J., Y. Deng, and G. Tóth (2006), The global ionosphere–thermosphere model, Journal of Atmospheric and Solar-Terrestrial Physics, Volume 68, Issue 8, 839-864.

Robinson, T. (1986), Towards a self-consistent non-linear theory of radar auroral backscatter, Journal of atmospheric and terrestrial physics, 48 (5), 417-422.

Schunk, R., and A. Nagy (2009), Ionospheres: physics, plasma physics, and chemistry, Cambridge university press.

Semeter, J., E. Macdonald, M. Hunnekuhl, M. Hirsch, N. Zeller, A. Chernenkoff, and J. Wang (2020), The Mysterious Green Streaks Below STEVE, Earth and Space Science, doi:10.1002/essoar.10502878.2

Schmeltekopf, A. L., E. E. Ferguson, and F. C. Fehsenfeld (1968), Afterglow studies of the reactions He^+, He (2^3S), and O^+ with vibrationally excited N_2, J. Chem. Phys., 48, 2966–2973.

Solomon, S. C., P. B. Hays, and V. J. Abreu (1988), The auroral 6300 Å emission: Observations and modeling, J. Geophys. Res., 93, 9867– 9882, doi:10.1029/JA093iA09p09867.

Solomon, S. C. (2017), Global modeling of thermospheric airglow in the far-ultraviolet, J. Geophys. Res., 122, doi:10.1002/2017/JA024314.

Spiro, R., R. Heelis, and W. Hanson (1979), Rapid subauroral ion drifts observed by Atmospheric Explorer C, *Geophys. Res. Lett.*, **6**, 657–660.

St-Maurice, J.-P., and Laneville, P. J. (1998), Reaction rate of O^+ with O_2, N_2, and NO under highly disturbed auroral conditions, *J. Geophys. Res.*, 103(A8), 17519– 17521, doi:10.1029/98JA01387.

St-Maurice, J.-P., & Goodwin, L. (2021). Revisiting the behavior of the *E*-region electron temperature during strong electric field events at high latitudes. *Journal of Geophysical Research: Space Physics*, 126, e2020JA028288. https://doi.org/10.1029/2020JA028288

St-Maurice, J.-P., C. Cussenot, and W. Kofman (1999), On the usefulness of E region electron temperatures and lower F region ion temperatures for the extraction of thermospheric parameters: a case study, Annales Geophysicae, 17 (9), 1182-1198.

Sydorenko, D., and Rankin, R. (2013), Simulation of O^+ upflows created by electron precipitation and Alfvén waves in the ionosphere, *J. Geophys. Res. Space Physics*, 118, 5562–5578, doi:10.1002/jgra.50531.

Thomas, G. E. (1963), Lyman α scattering in the Earth's hydrogen geocorona: 1., J. Geophys. Res., 68(9), 2639– 2660, doi:10.1029/JZ068i009p02639.

Richmond, A. D., E. C. Ridley, and R. G. Roble (1992), A thermosphere/ionosphere general circulation model with coupled electrodynamics, *Geophys. Res. Lett.*, **19**, 601–604, doi:10.1029/92GL00401

Wang, W., Talaat, E. R., Burns, A. G., Emery, B., Hsieh, S., Lei, J., and Xu, J. (2012), Thermosphere and ionosphere response to subauroral polarization streams (SAPS): Model simulations, *J. Geophys. Res.*, 117, A07301, doi:10.1029/2012JA017656.

Williams, P., B. Jones, and G. Jones (1992), The measured relationship between electric field strength and electron temperature in the auroral E-region, Journal of atmospheric and terrestrial physics, 54 (6), 741-748.

Yadav, S., Shiokawa, K., Otsuka, Y., Connors, M., & St Maurice, J.-P. (2021). Multi-wavelength imaging observations of STEVE at Athabasca, Canada. Journal of Geophysical Research: Space Physics, 126, e2020JA028622. https://doi.org/10.1029/2020JA028622.

Yeh, H.-C., J. C. Foster, F. J. Rich, and W. Swider (1991), Storm time electric field penetration observed at mid-latitude, J. Geophys. Res., 96(A4),5707–5721, doi:10.1029/90JA02751.

Zettergren, M., and Semeter, J. (2012), Ionospheric plasma transport and loss in auroral downward current regions, J. Geophys. Res., 117, A06306, doi:10.1029/2012JA017637.

Zhu, J., A. J. Ridley, and Y. Deng (2016), Simulating electron and ion temperature in a global ionosphere thermosphere model: Validation and modeling an idealized substorm, J. Atmos. So. Terr. Phys., 138, 243-260.

Zou, S., L. R. Lyons, and Y. Nishimura (2012), Mutual evolution of aurora and ionospheric electrodynamic features near the Harang reversal during substorms, *Geophysical Monograph Series*, *197*, 159–169, doi:10.1029/2011GM001163.

Figure Caption:

Figure 1. The slope of Te enhancement versus V_E for the AEH calculation used in this study.

Figure 2. (a) POES/NOAA-17 observations. The upper panel gives the Total Electron detector (TED) observations of the total electron precipitation fluxes; the bottom panel shows the energy channel where the differential electron fluxes maximize in the 0^0-sensor and 30^0-sensor (both sensors are within the loss cone). (b) Copied from Gillies et al. [2019] showing the optical spectra of STEVE compared to its ambient neighbors. (c) The 427.8 blue-line emission intensity derived from TREx spectrograph measurement as a function of MLAT. In (a) and (c), a vertical dashed line marks the position of STEVE arc.

Figure 3. Simulation outcome of altitude-MLAT profile of Te at six elapsed times. The latitudinal profiles of SAID and the background precipitation are plotted on top for reference. Zero relative latitude indicates the center of SAID.

Figure 4. Same as Figure 3 but for Ti.

Figure 5. Same as Figure 3 but for Ne.

Figure 6. Altitudinal profile of densities of Ne, NO+ and O+ at the center of SAID at (a) *t*=0; (b) t=1 min; (c) t=5 min; and (d) t=10 min. In subfigures (b)-(d), The initial (*t*=0) Ne profile is plotted in dotted line for reference.

Figure 7. Altitudinal profile of Pedersen conductivity at the center of SAID at (a) *t*=30 sec; (b) t=-2 min; (c) t=5 min; and (d) t=10 min. The initial (*t*=0) Pederson conductivity profile is plotted in dotted line for reference.

Figure 8. latitudinal profiles of Σ_P and FAC at different elapsed times. The latitudinal profiles of SAID and the background precipitation are plotted on top for reference.

Figure 9. Latitude-altitude profile of Ne, and the latitudinal profile of FAC at t=15 min for a new run with higher flow poleward of SAID. The latitudinal profiles of SAID and the background precipitation are plotted on top for reference.

Figure 10. Latitudinal profiles of plasma flows, Te, Ti, and Ne, averaged over 100-150 km altitudes.

Figure 1-10.

Figure 1

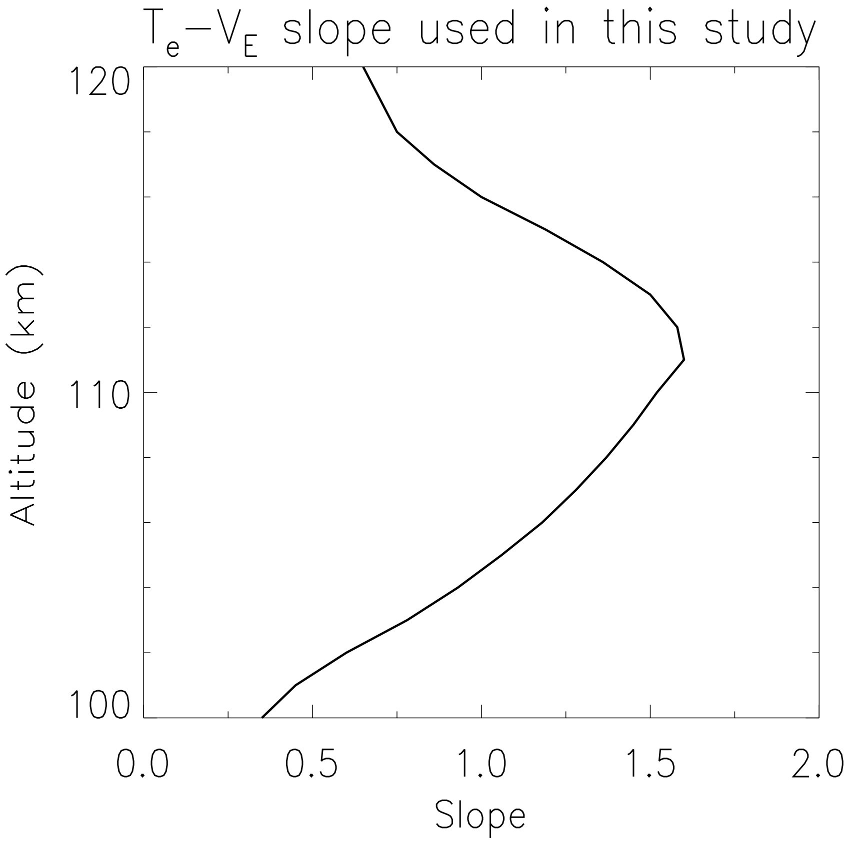

Figure 1. The slope of Te enhancement versus VE for the AEH calculation used in this study

Figure 2

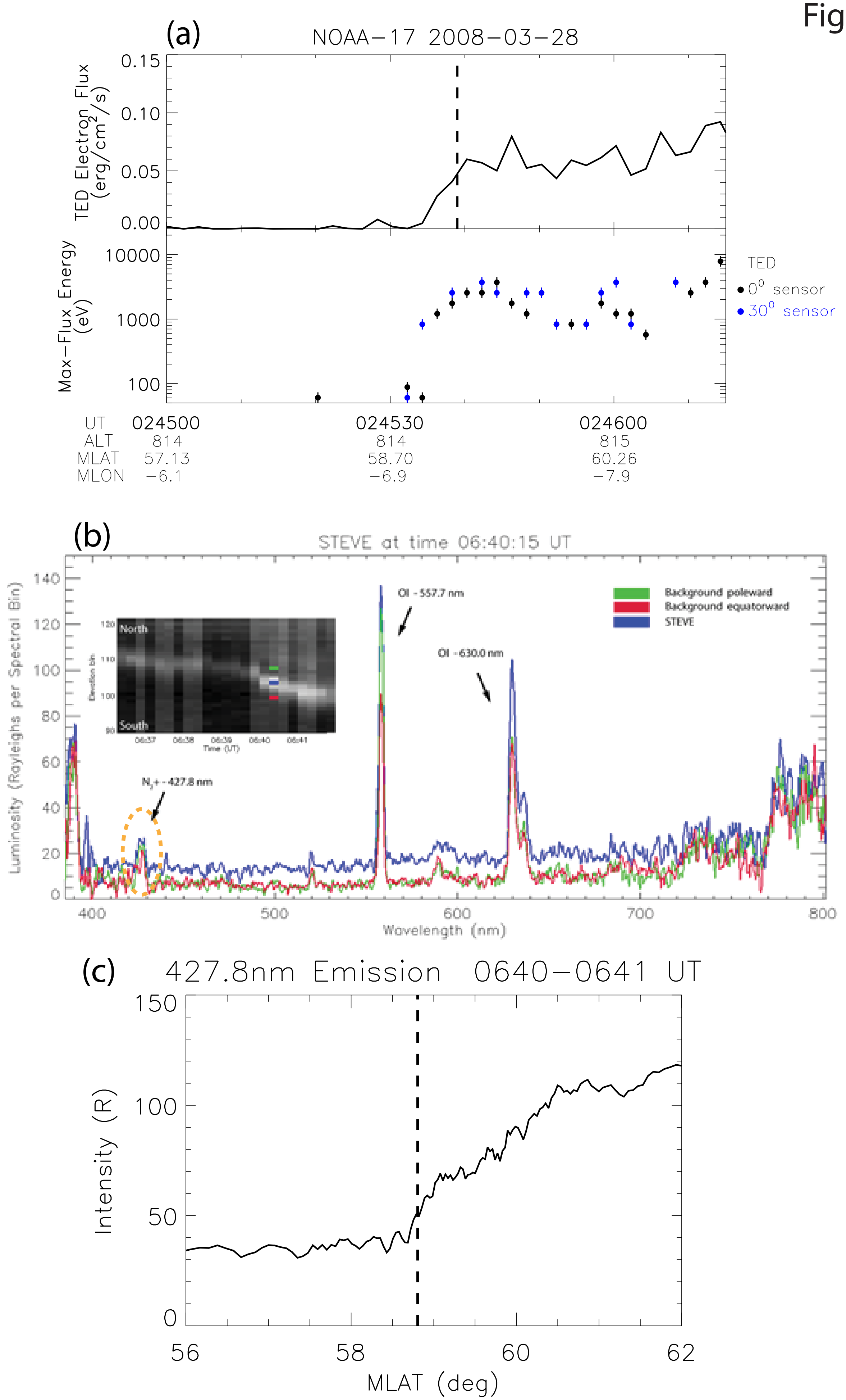

(a)
NOAA−17 2008−03−28
TED Electron Flux (erg/cm²/s)
0.15
0.10
0.05
0.00
Max−Flux Energy (eV)
10000
1000
100
TED
0⁰ sensor
30⁰ sensor
UT 024500 024530 024600
ALT 814 814 815
MLAT 57.13 58.70 60.26
MLON −6.1 −6.9 −7.9
(b)
STEVE at time 06:40:15 UT
Luminosity (Rayleighs per Spectral Bin)
OI - 557.7 nm
OI - 630.0 nm
N₂+ - 427.8 nm
Background poleward
Background equatorward
STEVE
North
South
Time (UT)
Wavelength (nm)
400
500
600
700
800
(c)
427.8nm Emission 0640−0641 UT
Intensity (R)
150
100
50
0
56
58
60
62
MLAT (deg)

Figure 2. (a) POES/NOAA-17 observations. The upper panel gives the Total Electron detector (TED) observations of the total electron precipitation fluxes; the bottom panel shows the energy channel where the differential electron fluxes maximize in the 00-sensor and 300-sensor (both sensors are within the loss cone). (b) Copied from Gillies et al. [2019] showing the optical spectra of STEVE compared to its ambient neighbors. (c) The 427.8 blue-line emission intensity derived from TREx spectrograph measurement as a function of MLAT. In (a) and (c), a vertical dashed line marks the position of STEVE arc

Figure 3

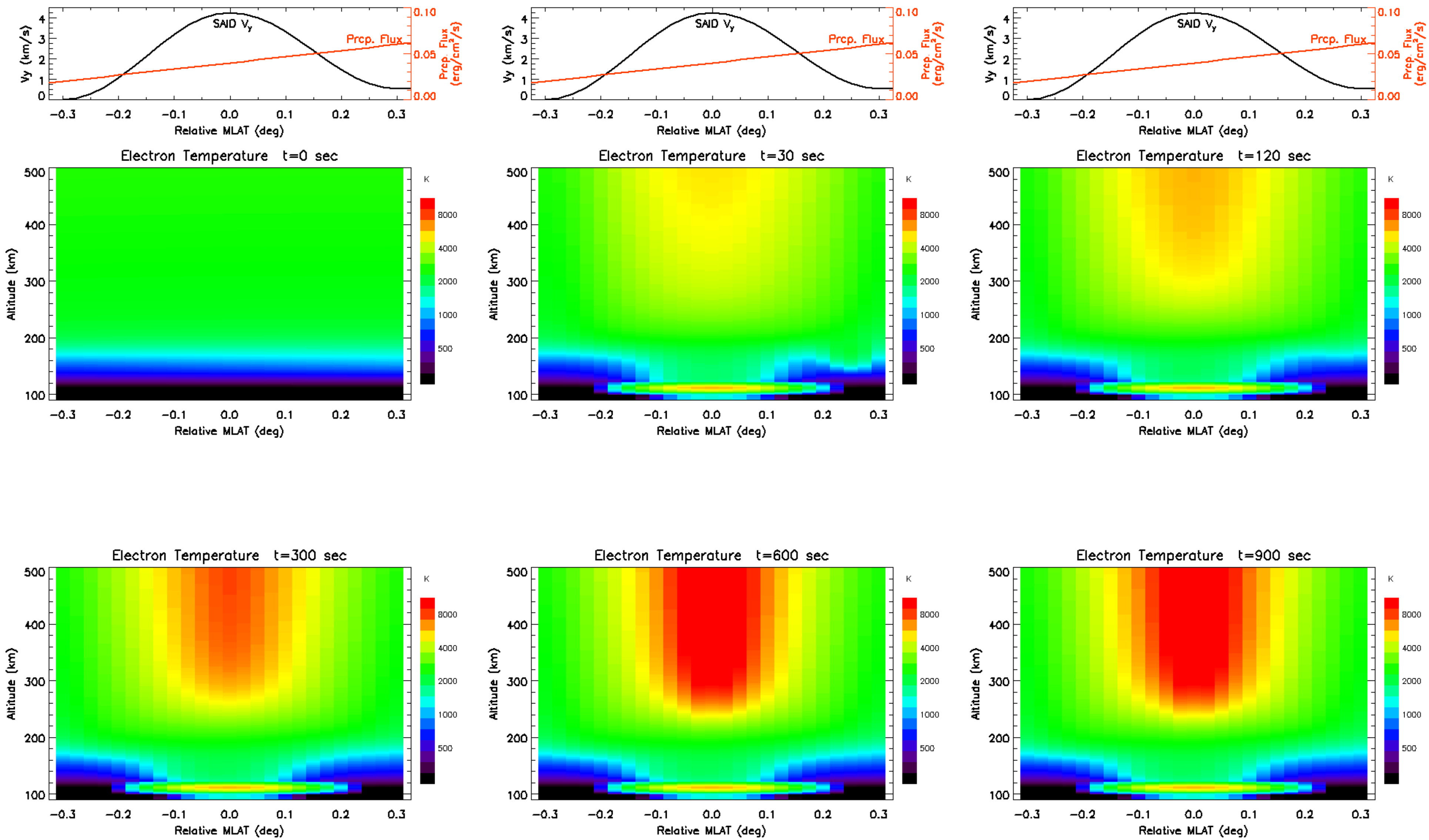

Figure 3. Simulation outcome of altitude-MLAT profile of Te at six elapsed times. The latitudinal profiles of SAID and the background precipitation are plotted on top for reference. Zero relative latitude indicates the center of SAID

Figure 4

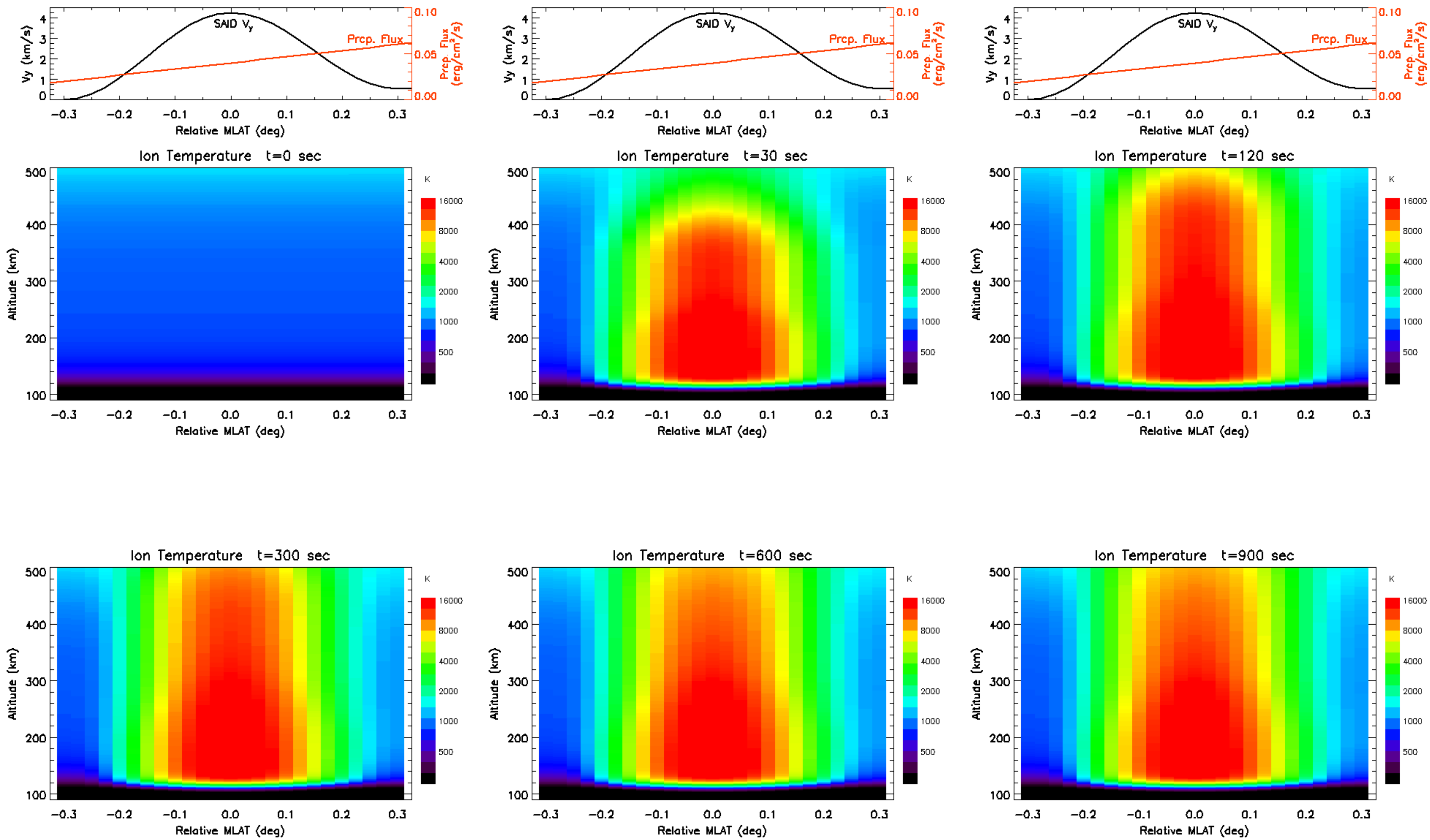

Figure 4. Same as Figure 3 but for Ti

Figure 5

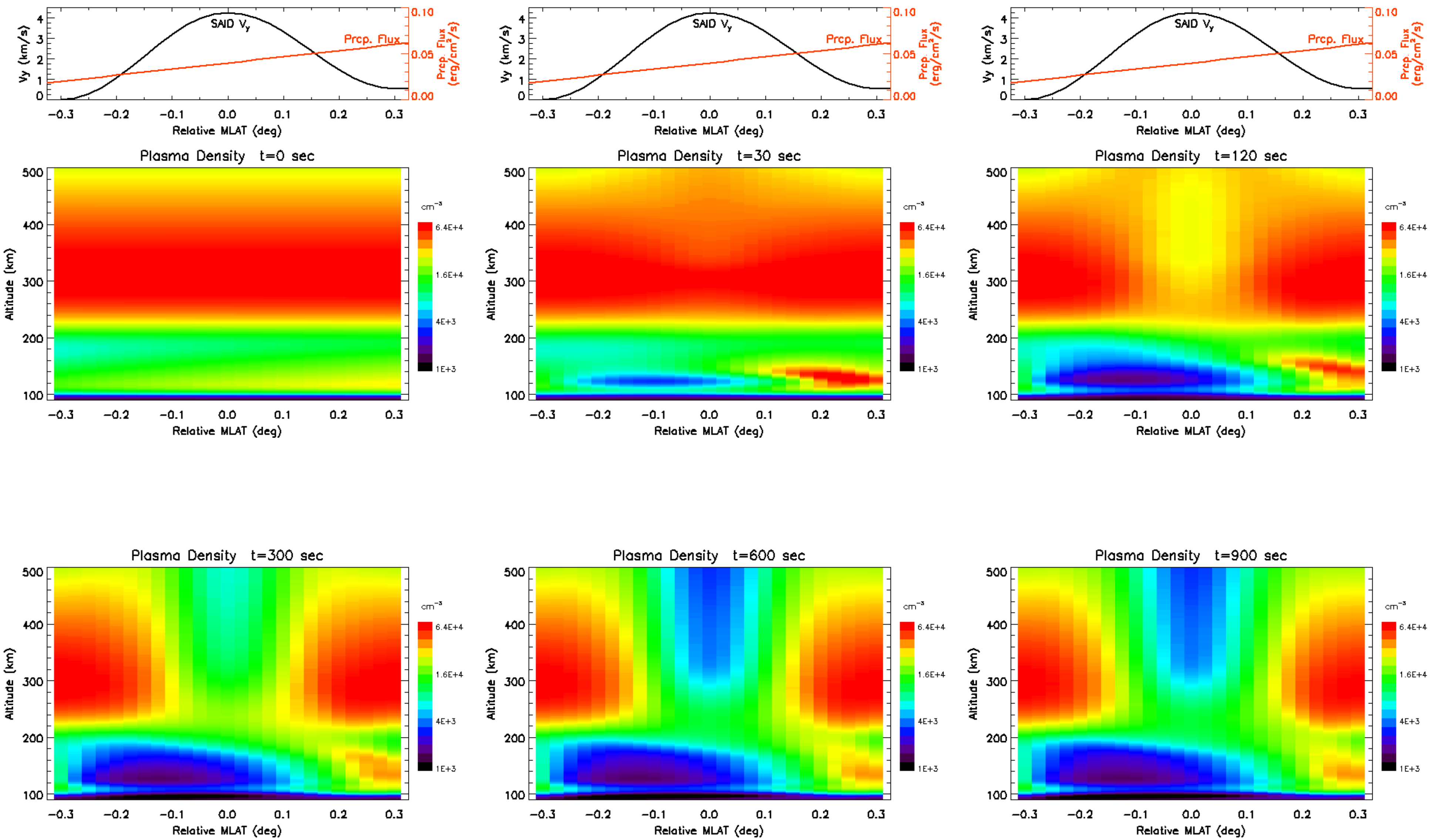

Figure 5. Same as Figure 3 but for Ne

Figure 6

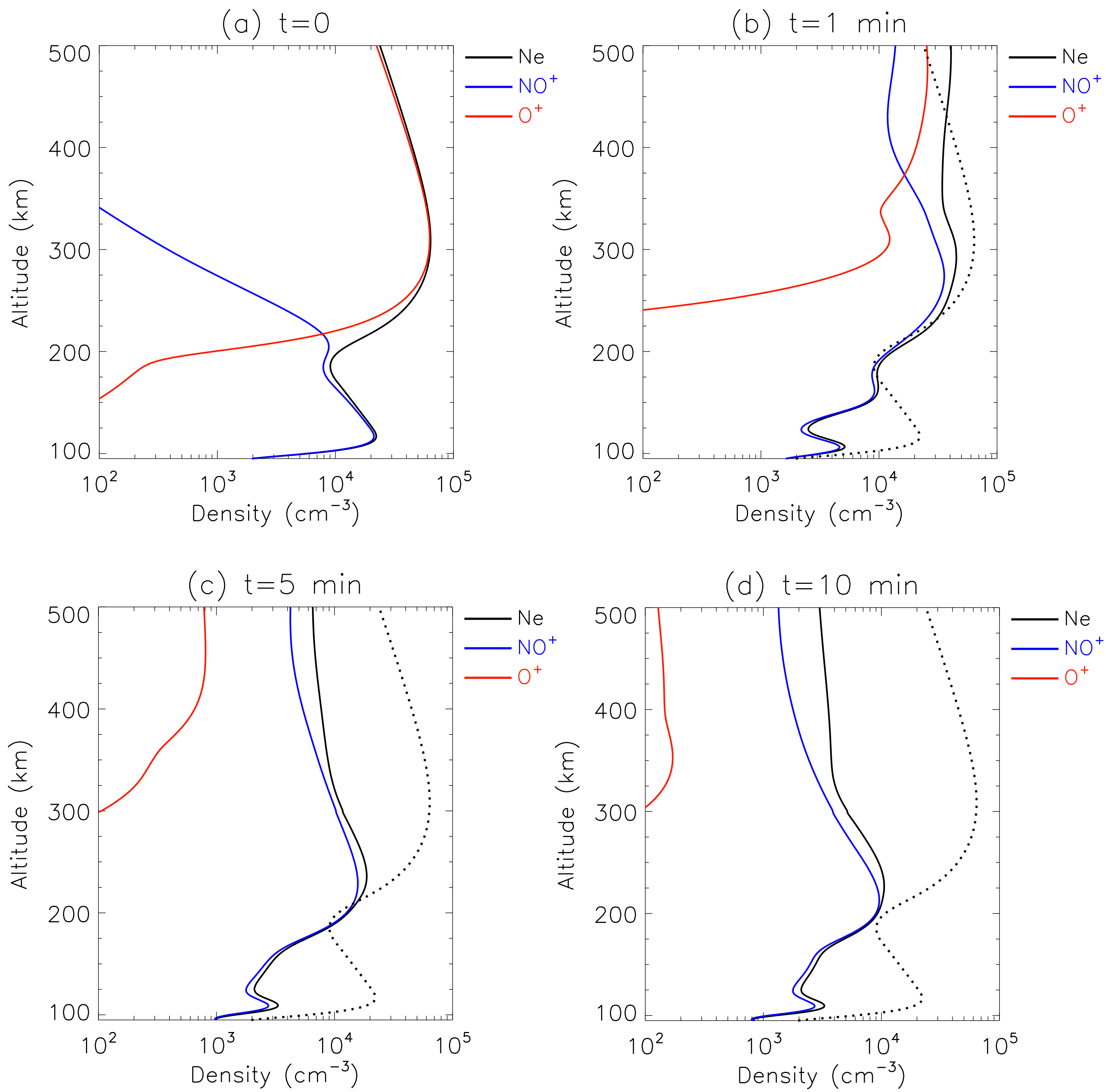

Figure 6. Altitudinal profile of densities of Ne, NO+ and O+ at the center of SAID at (a) t=0; (b) t=1 min; (c) t=5 min; and (d) t=10 min. In subfigures (b)-(d), The initial (t=0) Ne profile is plotted in dotted line for reference

Figure 7

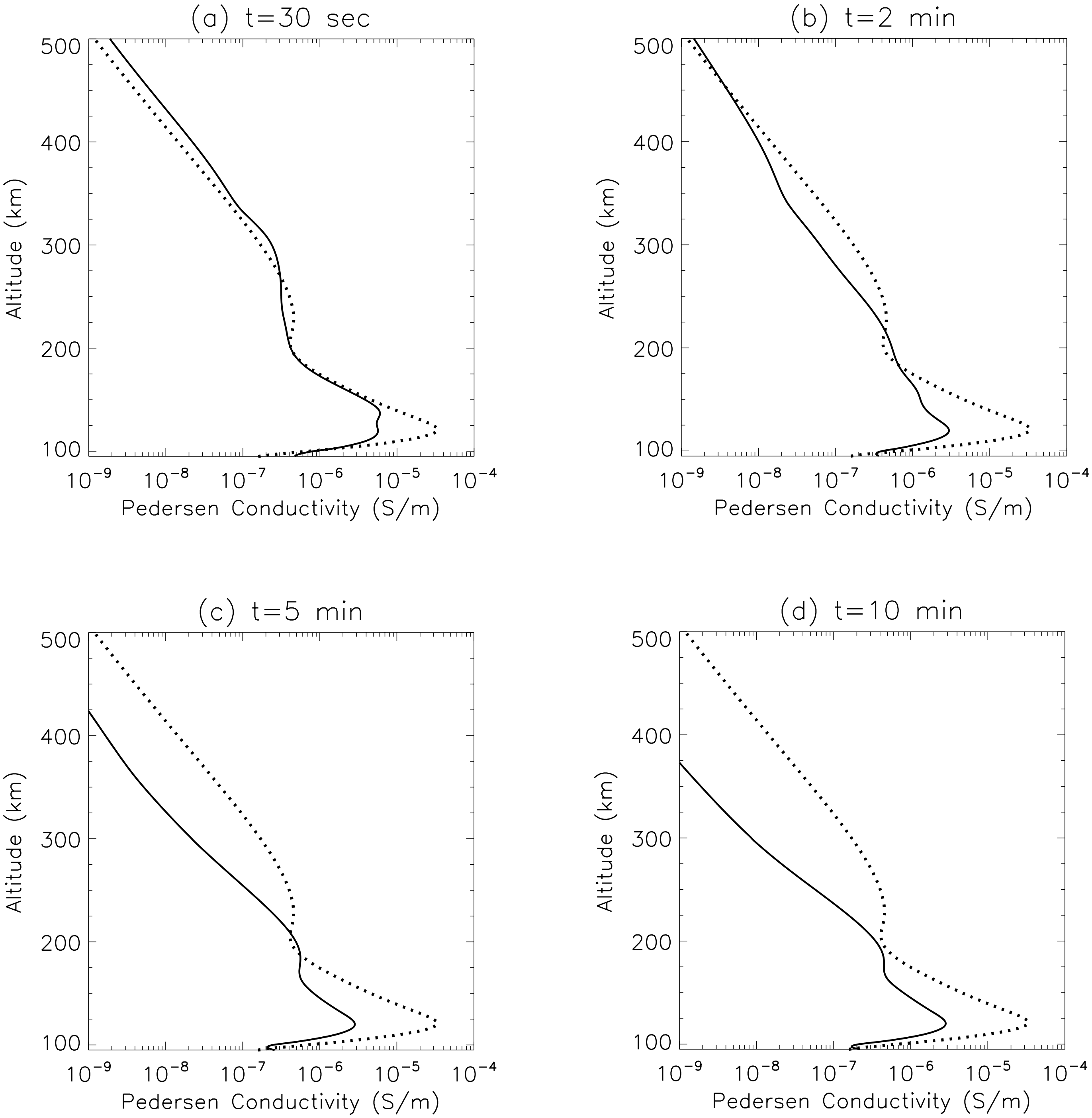

Figure 7. Altitudinal profile of Pedersen conductivity at the center of SAID at (a) t=30 sec; (b) t=-2 min; (c) t=5 min; and (d) t=10 min. The initial (t=0) Pedersen conductivity profile is plotted in dotted line for reference

Figure 8

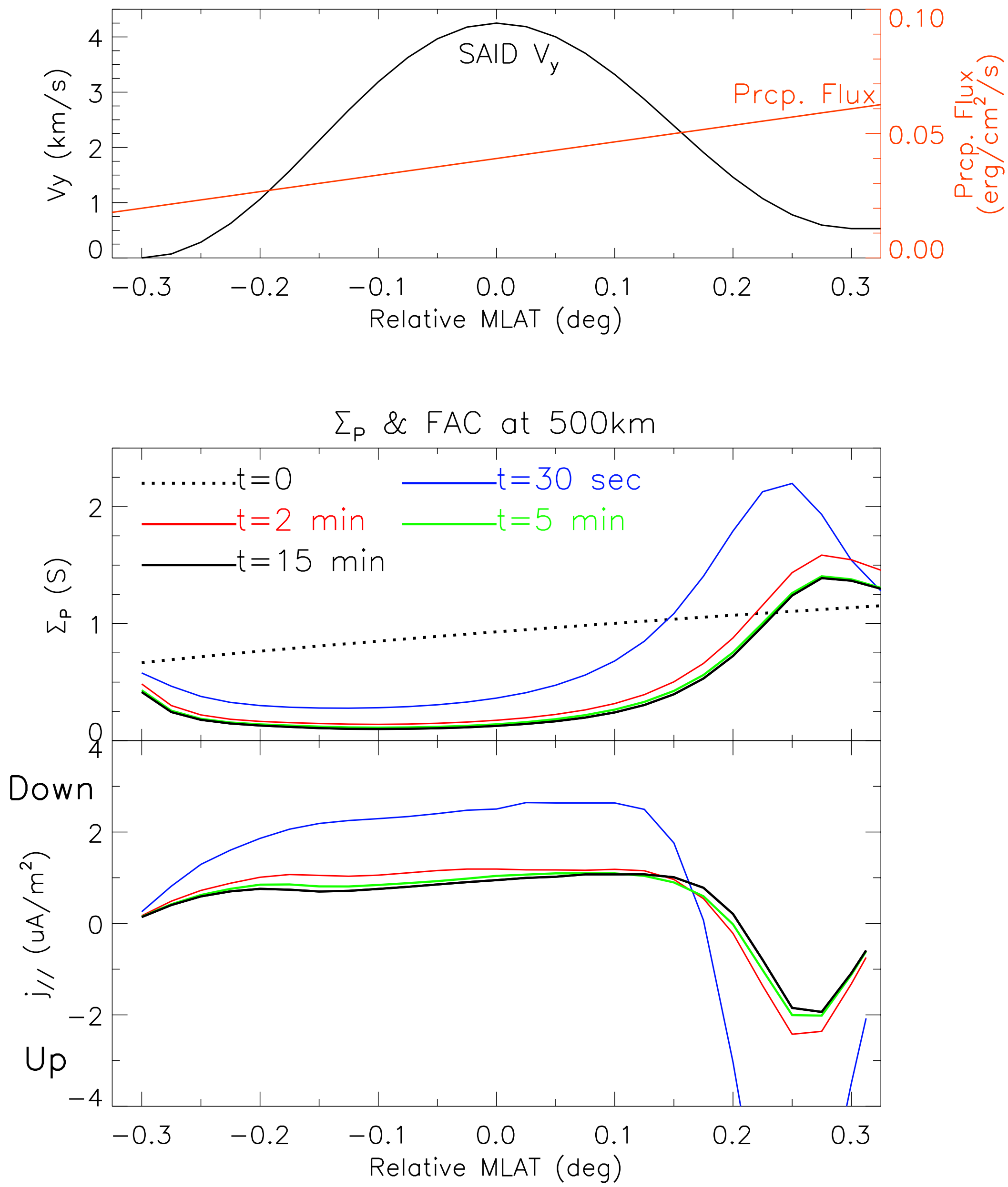

Figure 8. latitudinal profiles of Pedersen conductance and FAC at different elapsed times. The latitudinal profiles of SAID and the background precipitation are plotted on top for reference

Figure 9

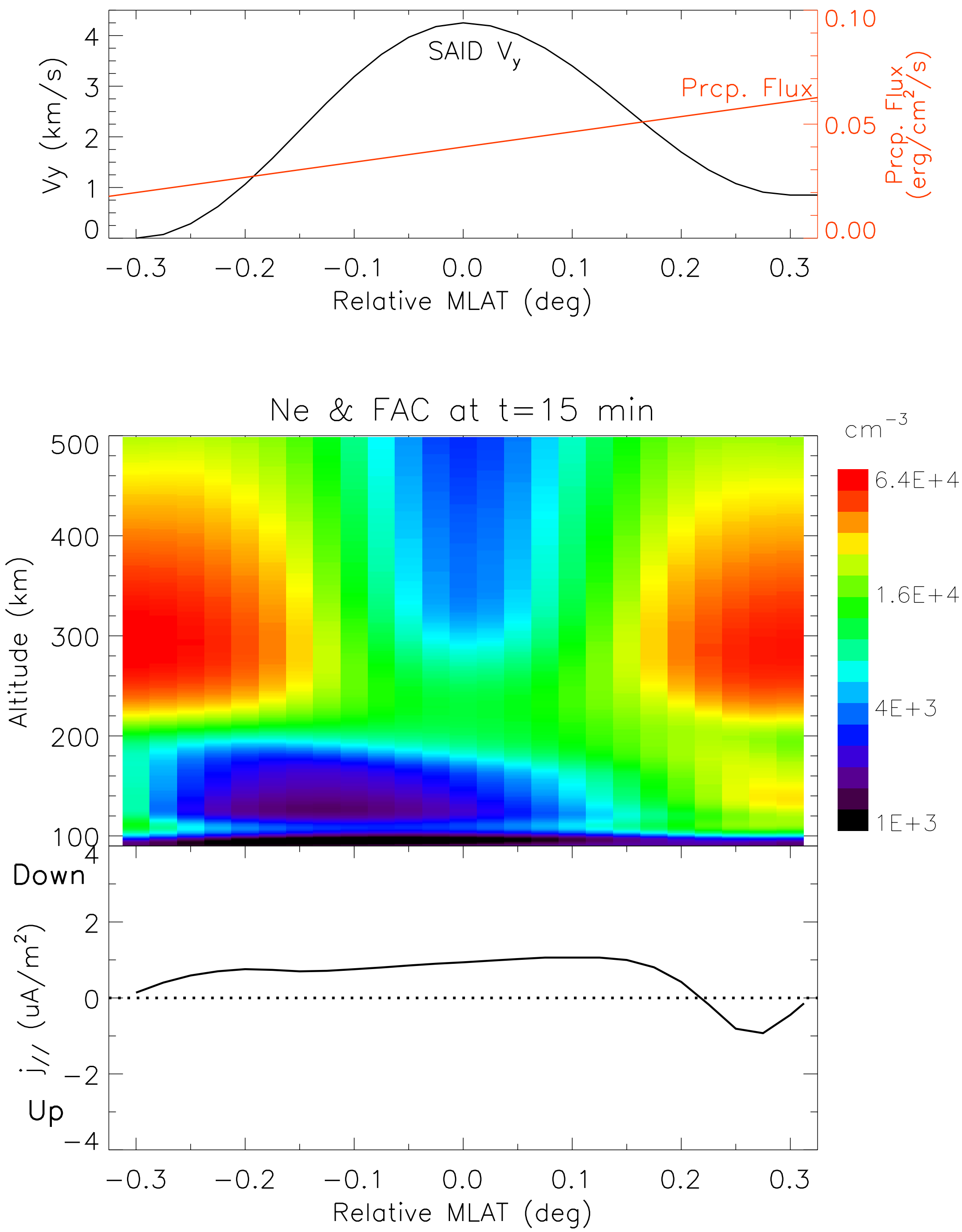

Figure 9. Latitude-altitude profile of Ne, and the latitudinal profile of FAC at t=15 min for a new run with higher flow poleward of SAID. The latitudinal profiles of SAID and the background precipitation are plotted on top for reference

Figure 10

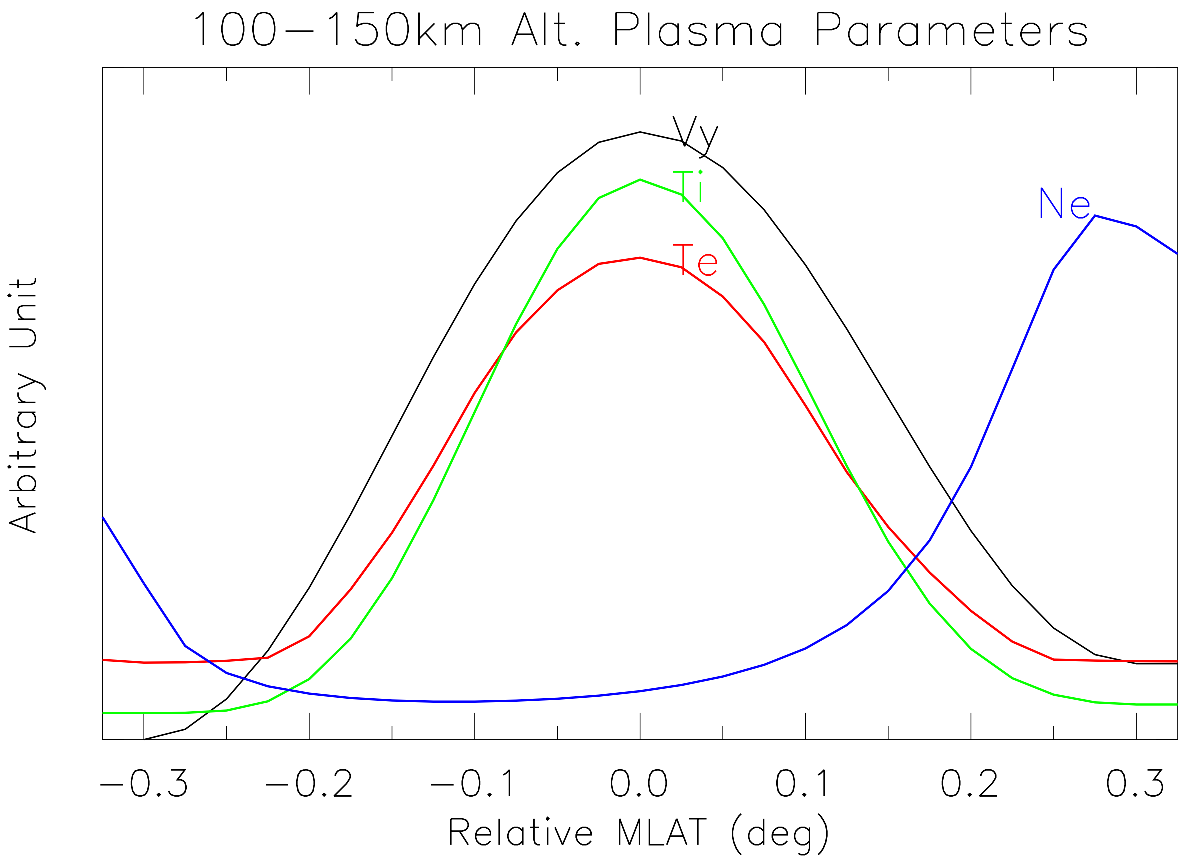

Figure 10. Latitudinal profiles of plasma flows, Te, Ti, and Ne, averaged over 100-150 km altitudes.